SUBMARINE CREVASSE LOBES CONTROLLED BY LATERAL SLOPE FAILURE IN TECTONICALLY-ACTIVE SETTINGS: AN EXHUMED EXAMPLE FROM THE EOCENE AÍNSA DEPOCENTRE (SPAIN)

Martinez-Doñate, A.[1], Soutter, E. L.[2], Kane, I.A.[2], Poyatos-Moré, M.[3], Hodgson, D.M.[4], Ayckbourne, A. J. M.[2], Taylor, W. J.[4], Bouwmeester, M. J.[2], Flint, S.S.[2]

1. Bureau of Economic Geology, Jackson School of Geosciences, The University of Texas at Austin, Austin, Texas

2. School of Earth and Environmental Sciences, University of Manchester, Manchester M13 9PL, UK.
3. Departament de Geologia, Universitat Autònoma de Barcelona, 08193 Cerdanyola del Vallés, Spain.
4. School of Earth and Environment, University of Leeds, Leeds LS29JT, UK.

ABSTRACT

Tectonic deformation and associated submarine slope failures modify seafloor relief, influencing sediment dispersal patterns and the resulting depositional architecture of deep-water systems. The exhumed Middle Eocene strata of the Banastón deep-water system in the Aínsa depocentre, Spain, allow the interplay between submarine slope confined systems, mass flow deposits, and syn-depositional compressional tectonics to be investigated. This study focuses on the Banastón II sub-unit, interpreted as low-sinuosity and narrow (2-3 km wide) channel-belt deposits confined laterally by opposing tectonically induced, fine-grained slopes. The studied succession (111 m-thick) is exposed along a 1.5 km long depositional dip-orientated (SE-NW) outcrop belt and documented here using facies analysis and physical correlation of 10 measured sections. Results show a stratigraphic evolution in which the channel axes migrated to the southwest, away from a growing structure in the northeastern part of the Aínsa depocentre. Uplift of the active margin promoted breaching of channel walls and confining slopes, with mass failures and the development of sand-rich crevasse scour-fills and crevasse lobes. We show that crevasse deposits form an important component of the overbank succession. These crevasse lobes are characterised by structureless thick and medium beds that form < 5 m thick packages in proximal parts and thin abruptly over 1 km into structured thin beds similar to the heterolithic dominated overbank deposits. Although development of crevasse lobes has been observed in multiple deep-water systems in ancient and modern systems, this study documents, for the first time, crevasse lobe development on the active compressional margins of a foreland basin rather than in the opposing and more stable and gentle margin. We discuss the mechanism for the formation of these crevasse deposits, which exploited the accommodation generated by the submarine landslides derived from the tectonically-active compressional margin.

INTRODUCTION

Submarine slope canyons and channel systems are conduits for the delivery of sediment (Mutti and Normark, 1991; Piper and Normark, 2001), nutrients (Heezen *et al.*, 1955) and pollutants (Kane and Clare, 2019; Zhong and Peng, 2021) to deep-water. Submarine channel belts result from erosional degradation of the slope and/or aggradation of constructional overbank deposits (Buffington, 1952; Menard, 1955; Normark, 1970). Sediment-gravity-flows travelling downslope are partially confined within the channels, with the more dilute and finer fraction of flows spilling and depositing onto overbank areas (Piper and Normark, 1983; Peakall et al., 2000; Keevil et al., 2006; Kane et al., 2007; Kane and Hodgson, 2011; Hansen et al., 2017a). When these flows are unconfined, wedge-shaped external levees are constructed and provide channel confinement (Buffington, 1952; Kane and Hodgson, 2011). However, limited accommodation in confined depocentres, such as in peripheral foreland basins, like the Aínsa Basin, hinders the construction of external levees and instead these systems develop confined overbank wedges bound by the lateral slope(s) (De Ruig and Hubbard, 2006; Hubbard et al., 2009). Breaching of channel margins or external levees can lead to crevasse scours and lobe deposition and can ultimately result in avulsion of the channel (Damuth et al., 1988; Posamentier and Kolla, 2003; Fildani and Normark, 2004; Armitage et al., 2012; Brunt et al., 2013; Maier et al., 2013; Morris et al., 2014). While the large-scale morphology of structurally-confined submarine slope channel systems can be resolved with seismic reflection data, the distribution and decimetre- to metre-scale architecture of sand-prone elements within otherwise mudstone-dominated confined overbank settings are rarely resolvable. In addition, known examples of exhumed crevasse scour-fills and lobes are rare, and therefore their high-resolution sedimentology and stratigraphic architecture is sparsely documented.

Sediment routing systems and deep-water stratigraphic patterns in small, active foreland basins largely depend on the basin physiography, which is often characterised by opposing laterally confining slopes and influenced by the uplift/movement of compressional structures. Submarine channels in these settings are characterised by low sinuosity (Bayliss & Pickering, 2015), and avulsion mechanisms are less understood than in highly sinuous, unconfined channel systems. The longitudinal profile, evolution and architecture of submarine channels in tectonically-active compressional settings, therefore, tend to be primarily controlled by pre- or syn-depositional tectonic relief (Heiniö and Davies, 2007; Kane et al., 2010; Tinterri and Muzzi Magalhaes, 2011; Georgiopoulou and Cartwright, 2013), halokinesis (Beaubouef & Friedmann, 2000; Gee & Gawthorpe, 2006; Kane *et al.*, 2012) and the emplacement of submarine landslides (Canals et al., 2000; Pickering and Corregidor, 2005; Tinterri and Muzzi Magalhaes, 2011; Fairweather, 2014; Kneller et al., 2016; Kremer et al., 2018; Nwoko et al., 2020; Tek et al., 2020; Steventon et al., 2021; Tek et al., 2021). Hereafter, the term submarine landslide will refer to a remobilised sedimentary body translated downslope due to gravitational instabilities and deposited en-masse (Nardin et al., 1979; Hampton et al., 1995; Mulder and Alexander, 2001; Moscardelli and Wood, 2008; Bull et al., 2009; Talling et al., 2012; Kneller et al., 2016).

The exhumed Eocene deep-water strata of the Aínsa Basin show well-preserved examples of submarine slope channel-fill deposits in an active collisional foreland basin setting (Fig. 1A). Here, the growth and propagation of structures related to the Pyrenean orogeny, controlled the formation and migration of successive deep-water systems (e.g., Pickering and Corregidor, 2005; Arbués et al., 2007; Pickering and Bayliss, 2009; Dakin et al., 2013; Cantalejo and Pickering, 2014; Bayliss and Pickering, 2015; Scotchman et al., 2015a; Castelltort et al., 2017; Bell et al., 2018; Tek et al., 2020). This field-based study focuses on the part of the Banastón system (Banastón II sub-unit; Fig. 1B) that crops out in the San Vicente area, north of Aínsa (Fig. 1C). The Banastón II sub-unit is well-exposed in a 111 m-thick succession along a 1.5 km long depositional dip-orientated (SE-NW) outcrop belt. The objectives of this study are to 1) improve our understanding of the different sub-environments of deposition and architecture of slope channel-fill deposits at bed scale; 2) document the controls and sedimentary processes involved in crevasse lobe development; and 3) evaluate the role that active tectonism and mass-wasting processes played in the evolution and avulsion of the Banastón deep-water system.

GEOLOGICAL SETTING

Late Cretaceous to Miocene convergence between the Eurasian and Iberian continental plates resulted in the formation of the Pyrenees (Srivastava & Roest, 1991; Muñoz, 1992; Muñoz, 2002; Rosenbaum *et al.*, 2002), and their related north and south Pyrenean peripheral foreland basins (Fig. 1A). The southern foreland basin was characterised by a southward-verging thin-skinned fold-and-thrust system, which led to the development of a WNW-ESE orientated and westward deepening, narrow and elongated foredeep to piggyback depocentres (Muñoz, 1992, 2002; Dreyer *et al.*, 1999). Typically, the south-central foreland basin is subdivided into three main sectors, which formed a linked source-to-sink system during the Lower to Middle Eocene (Nijman, 1998; Payros *et al.*, 2009; Chanvry *et al.*, 2018): i) the Tremp-Graus depocentre in the east, with alluvial, fluvio-deltaic and shallow-marine deposits; ii) the Aínsa depocentre in the central part, dominated by submarine slope deposits; and iii) the Jaca depocentre in the west, where basin floor deposits are found. The deep-water deposits of the Aínsa and Jaca depocentres are collectively known as the Hecho Group (Mutti *et al.*, 1972) and have been the focus of many studies (e.g. Barnolas & Gil-Peña, 2002; Remacha & Fernández, 2003; Pickering & Corregidor, 2005; Arbués *et al.*, 2007; Payros *et al.*, 2009; Pickering & Bayliss, 2009; Clark & Cartwright, 2011; Castelltort *et al.*, 2017). The turbiditic systems of the Hecho Group were predominantly fed by fluvio-deltaic environments in the east (Fontana et al., 1989; Gupta and Pickering, 2008; Caja et al., 2010; Thomson et al., 2017), supplying the Aínsa depocentre through a series of tectonically-controlled submarine canyons and channel systems (Mutti, 1977; Puigdefàbregas and Souquet, 1986; Millington and Clark, 1995).

In the Aínsa depocentre, seven deep-water systems have been recognized from older to younger: Fosado, Arro, Gerbe, Banastón, Aínsa, Morillo and Guaso (Burbank et al., 1992;

Payros et al., 2009; Poyatos-Moré, 2014; Bayliss and Pickering, 2015; Scotchman et al., 2015; Castelltort et al., 2017; Clark et al., 2017). This study focuses on the Lutetian-aged Banastón system; the cumulative thickness ranges from ~500 m on the upper slope to ~700 m on the lower slope (Bayliss and Pickering, 2015). The channelised system was characterised by an axial supply (NNW-directed palaeoflow) with a lateral-offset stacking pattern towards the WSW (Fig. 1B). This progressive migration of channel axes towards the WSW was controlled by the syn-depositional growth and propagation of NW-SE oriented oblique-lateral ramp structures related to more regional E-W thrust sheets. (Poblet *et al.*, 1998; Fernández *et al.*, 2012; Muñoz *et al.*, 2013).

Bayliss and Pickering (2015) mapped six channelised sandstone bodies within the Banastón system: Banastón I (BI: 149 m thick and 2000 m wide), Banastón II (BII: 98m thick and 1800 m wide), Banastón III (BIII: 72 m thick and 1700 m wide), Banastón IV (BIV: 124 m thick and 2500 m wide), Banastón V (BV: 97 m thick and 3300 m wide), and Banastón VI (BVI: 160 m thick and 2400 m wide) (**¡Error! No se encuentra el origen de la referencia.**B). These six channelised sandstone bodies were subdivided into Stage 1 (BI-BIII) and Stage 2 (BIV-BVI) by Bayliss and Pickering (2015), where BI, BII and BIII were confined between the Mediano and Añisclo anticlines, and BIV, BV and BVI between the Añisclo and Boltaña anticlines, forming two NNW-oriented ~5-8 km wide corridors. This study focuses on the Banastón II sub-unit, whose deposition has been linked to a period of active compressional tectonics in the basin (Läuchli *et al.*, 2021).

DATA AND METHODS

We investigated the sedimentology, and stratigraphic architecture of a 111 m-thick section in the Banastón II sub-unit over a 1.5 km SW-NE orientated outcrop belt. The structural bedding within the studied succession dips at 30° to the SSW. We collected 10 detailed sedimentary logs (Fig. 1C) at a 1:20 scale to document bed thickness, lithology, sedimentary structures, textures and palaeocurrent measurements (n=73) from ripple foresets, flute marks, and groove casts. Sedimentary logs were correlated by walking out individual sandstone packages, enabling the vertical and lateral characterization of different facies associations and the general stratigraphic evolution of the Banastón II system in the study area. Additionally, 7 detailed logs were collected at a 1:2 scale to document the complexity and fine-scale thickness variability of specific stratigraphic intervals. The sandstone-mudstone proportion was analysed and plotted using the *Striplog* Python package from *Agile Geoscienc*e© (https://code.agilescientific.com/striplog/index.html). Additionally, Uncrewed Aerial Vehicle (UAV) photogrammetric models were built to capture the stratigraphic architecture of stratal packages in inaccessible areas.

FACIES ASSOCIATIONS

Based on facies and outcrop analysis, we recognised 14 lithofacies in the Banastón II sub-unit (Figs. 2, 3, 4, Tables 1 and 2). These lithofacies have been grouped into 5 facies associations (Fig. 5), representing different depositional sub-environments.

FA1: Overbank deposits

Description: This facies association is characterised by thin-bedded heterolithic < 20 m thick successions (Fig. 5A) dominated by alternating structureless carbonate mudstones (Lf1) and thin-bedded siltstones and sandstones (Fig. 2A). Some thin siltstone and sandstone beds have flat to loaded bases and lenticular geometries, and may pinch out laterally (Lf2a) or are laterally extensive (Lf2b) over tens of metres (Fig. 2A and Fig. 2B). Lf2a is structureless or comprises starved-ripple cross-lamination (Fig. 2A) indicating NW-directed palaeoflows, while Lf2b shows planar lamination (Fig. 2B). Locally, the conformable bedding of FA1 can be interrupted by unconformable 0.5-7 m thick deformed thin-bedded packages, rotated above south-westwards dipping concave-up planes (Lf7a and Lf7b; Figs. 4A-4C). Lf7a is thinner than 5 m and shows limited disaggregation, with minor deformation in the bedding (Figs. 4A and 4B). However, Lf7b is 5-7 m thick, and the bedding is deformed and comprises metre-scale fold amplitudes (Fig. 4C).

Interpretation: The development of FA1 is the result of combined deposition from dominantly background sedimentation and low-density fine-grained turbidity currents. Here, background sedimentation refers to hemipelagic settling, and thin dilute sediment gravity flow deposits not visible to the naked eye in outcrop (Boulesteix *et al.*, 2019, 2020, 2022). These accumulations of thin beds are interpreted as the product of flow-stripping of the dilute upper parts of channelised turbidity currents into the overbank areas (Piper and Normark, 1983; Peakall et al., 2000; Keevil et al., 2006; Kane et al., 2007; Kane and Hodgson, 2011; Hansen et al., 2017a). When these flows exit the confining channel belt, they are characterised by capacity-driven deposition as they become less confined (Hiscott, 1994a; Hübscher et al., 1997; Posamentier and Kolla, 2003; Kane et al., 2007, 2010b) causing rapid deceleration and the development of transitional behaviour from initially turbulent flows to more laminar flows (e.g. Lf3b). Rotated stratigraphy is also a common feature of overbank environments adjacent to channels (e.g. Kane et al., 2007; Kane et al., 2011; Dykstra et al., 2007; Hubbard et al., 2009; Hansen et al., 2015) and represents localised submarine landslide deposits of nearby stratigraphy such as from draping and accretion on steep bounding slopes (Abreu et al., 2003; De Ruig and Hubbard, 2006; Hubbard et al., 2009) where the channel belt is confined.

FA2: Terrace deposits

Description: This facies association is characterised by medium-bedded heterolithic <5 m thick successions (Fig. 5B), with a basal matrix-supported conglomerate (Lf7c; Figs. 4D and 4E), overlain by an alternation of carbonate mudstone (Lf1; Fig. 2A) and thin- to medium-bedded sandstones with a wide grain size range from fine to pebbly sand (Fig. 5B). Deformed heterolithic packages rotated above concave-up planes are also observed (Lf7a; Figs. 4A and 4B). Some medium-bedded sandstones show rounded, convex-up tops that exhibit positive relief up to 10 cm, which also pinchout laterally over several metres (Lf3a; Fig. 2C). This facies association also comprises medium-bedded tabular sandstones with sharp flat bases and sharp wavy tops (Lf3b; Fig. 2D). Commonly, Lf3b is structureless at the base with well-developed planar lamination towards the top. In addition to the lithofacies described above, FA2 is differentiated from FA1 by dune-like lenticular bodies and associated scour surfaces (see Soutter et al., *in review*). Dune-forming beds are structureless or comprise faintly planar laminated basal divisions that pass vertically into a normally graded well sorted granular to pebbly sandstone division (Lf6; Figs. 3C, 3D and 3E) with well-developed foresets, characterised by abundant mudstone clasts dipping consistently towards the NNW (Fig. 3C). Foresets are commonly overlain by a grain-size break and a finer-grained ripple laminated division which represent the top division (see Soutter et al., *in review*), indicating NW-directed palaeoflows. Bed tops are characterized by intense bioturbation (Thalassinoides; Fig. 3F). Furthermore, Lf6 dune-forming beds exhibit a distinctive reddish colour and, in plan view, develop crescentic-shaped profiles (Fig. 3D) (Soutter et al., *in review*). Lf6 overlies matrix-supported conglomerate (Lf7c) and becomes less frequent toward the top of the FA2 stratal packages.

Interpretation: The variability in deposit thickness and grain size range in the FA2 deposits suggests an environment of deposition dominated by flows of variable magnitudes. The thin-bedded siltstones reflect deposition from overspilling and flow stripping of lower magnitude flows (Peakall *et al.*, 2000; Dennielou *et al.*, 2006; Hansen *et al.*, 2015). On the other hand, the sandstones and coarse-grained dune-like deposits indicate deposition from steady (Kneller and Branney, 1995) and bypassing high magnitude energetic flows, which reworked a previously deposited coarser fraction (Amy *et al.*, 2000; Stevenson *et al.*, 2015; Hansen *et al.*, 2021). Furthermore, the lack of channel-scale erosional features within these packages suggests that FA2 corresponds to terrace deposits formed on a relatively flat to shallow surface in an elevated position relative to the active channel, yet still inside the channel belt (Babonneau et al., 2002, 2004, 2010; Hansen et al., 2015, 2017a, 2017b; Allen et al., 2022). The basal matrix-supported conglomerates (Lf7c; Fig. 5B) are considered local deposits of cohesive debris flows (Talling *et al.*, 2012), which might create a relative topographic high with certain rugosity and form the initial terrace surface. The deformed heterolithic units (Lf7a) are attributed to gravitational failures of the channel walls and/or adjacent confining slopes (Hansen et al., 2015, 2017b; Allen et al., 2022).

FA3: Channel-fill deposits

Description: FA3 comprises a 5-15 m thick package (Fig. 5C) dominated by highly amalgamated thick-bedded sandstones, commonly overlying a basal muddy, matrix-supported, extrabasinal clast-bearing conglomerate (Lf7c; Figs. 4D and 4E). The thick sandstone beds are weakly normally graded, commonly structureless, and feature NNW-directed flutes, with locally developed planar and NNW-dipping ripple lamination (Lf4a; Fig. 1F). In the lower half of FA3, where not amalgamated, the thick beds of Lf4a show silty tops and are bounded by heterolithic packages (<0.3 m) of Lf1 and Lf2b (Fig. 5C). In the upper half, they develop unconformable bases that incise (up to 0.5 m) into the underlying stratigraphy, with abundant scours, mudstone clasts and grain-size breaks (Fig. 5C).

Interpretation: The basal matrix-supported conglomerates represent deposition from cohesive debris flows. The amalgamation and weak normal-grading within thick beds indicate deposition from high-density turbidity currents (*sensu* Lowe, 1982) under high aggradation rates (Kneller and Branney, 1995; Sumner et al., 2008). Furthermore, the silty tops of the thick beds in the lower half of FA3 suggest an abrupt loss in capacity and competence and deposition under high deceleration rates. In contrast, the scouring, abundance of mudstone clasts, and grain-size breaks reported in the upper half suggest sediment bypass and erosional flows (Stevenson *et al.*, 2015). These stratal packages are therefore interpreted as deposits from channelised flows. However, the lack of major erosional surfaces (at the exposure scale) and minor bypass indicators suggest that FA3 is more closely related to channel backfilling than being representative of early channel formation, i.e. erosion and almost complete bypass (Hodgson *et al.*, 2016), while the basal surface of the matrix-supported conglomerates (here interpreted as debrites rather than lag deposits) would indicate the base of the channel.

FA4: Crevasse scour-fill deposits

Description: This facies association comprises a <5 m thick succession (Fig. 5D) of highly amalgamated sandstone beds interbedded with sheared mudstone intervals (Lf7d). Medium- to thick-bedded sandstones (Lf5) with poor lateral continuity (<100 m long) and low aspect ratios (5:1 to 10:1, width: thickness) characterise this facies association (FigA and FigB). Scours bound the base of Lf5 and Lf7d (<2 m thick), truncating underlying beds (Fig. 5D). Lf5 sandstone beds are planar or cross-bedded, medium- to coarse-grained with grain-size breaks, comprising abundant mudstone clasts orientated parallel to the laminae and centimetre-scale grooves at bed bases (Figs. 3A and 3B). Lf5 sandstone beds comprise grooves with high divergence in contrast to the flutes and the cross-bedding, which consistently indicate NNW-oriented palaeoflow. Abundant centimetre- to decimetre-scale burrows are observed, preferentially at the base of the thick-bedded sandstone (Fig. 3A) or elongated (5-50 cm long) from top to base at sheared mudstone intervals (Lf7d; Fig. 4).

Interpretation: Lf5 sandstone and Lf7d mudstone beds represent small-scale scour-fills (Arnott and Al-Mufti, 2017), while the truncation and low aspect ratio beds observed at their base support scouring of the substrate by previously bypassing flows (Pemberton et al., 2016; Terlaky and Arnott, 2016; Hofstra et al., 2018; Pohl et al., 2020). The deposition of crudely-graded to ungraded (Lf5) sandstones over the scour surfaces is interpreted as the product of high sedimentation rates from high-density turbidity currents (*sensu* Lowe, 1982), suppressing tractional reworking and, therefore, consistent with crevasse-related sedimentation. The development of grain-size breaks, cross-bedding and mudstone clast horizons in Lf5 indicates partial bypass by sustained flows (Kneller & McCaffrey, 2003; Kane *et al.*, 2009; Stevenson *et al.*, 2015). The sheared mudstones (Lf7d) indicate compression along the front of localised, small-scale failures of nearby fine-grained stratigraphy (Ayckbourne *et al.*, 2022). The intense burrowing supports sustained high oxygen and nutrient levels, suggesting proximity to channels.

FA5: Crevasse lobe deposits

Description: This facies association forms a medium- to thick-bedded tabular sandstone package (1.5–5 m thick; Fig. 5E). The dominant lithofacies are thick-bedded, structureless, crudely-graded sandstones (Lf4b; Fig. 2G). Lf4b is characterised by abundant decimetre-scale burrows and silty tops (Figs. 2G and 2H; e.g. Morris et al., 2014a). When not amalgamated, thick beds are bounded by 1-30 cm thick mudstone intervals (Lf1) or thin- to medium-bedded planar laminated sandstones (Lf2b and Lf3b; Figs. 2B and 2D) or stoss-side preserved climbing ripples (Lf3c; Fig. 2E).

Interpretation: The Lf4b lithofacies within this association suggest rapidly deposited medium- to high-density turbidity currents (*sensu* Lowe, 1982). Silty tops can be related to an abrupt loss in flow capacity (Hiscott, 1994) due to rapid unconfinement as it exits the crevasse channel/scours. Planar laminations and stoss-side preserved climbing ripples indicate continued bedload traction with high aggradation rates (Sorby, 1859, 1908; Allen, 1973; Jobe, 2012). The intense bioturbation is consistent with proximity to channels, suggesting that these high aspect ratio sand-rich packages are frontal or crevasse lobes (e.g. Morris et al., 2014a, b). The mapping of Bayliss and Pickering (2015) shows that these lobes developed at the flanks of the channel belt rather than at its mouth. Furthermore, they overlie the Banastón II channel-fills and terrace deposits, supporting the interpretation that they represent crevasse lobes rather than frontal lobes (e.g. Beaubouef, 2004; De Ruig and Hubbard, 2006; Hubbard et al., 2009; Morris et al., 2014b).

DEPOSITIONAL ARCHITECTURE

The five facies associations (FA1-FA5) described above stack to form two major architectural elements: i) channel belts and ii) structurally confined overbank deposits (Figs. 6 and 7).

Channel belt

Both terrace deposits (FA2) and channel-fill deposits (FA3) suggest deposition within a partly confined/channelised environment, referred to as a channel belt. The mapping from Bayliss and Pickering (2015) and the relatively low divergence in palaeocurrent directions (Fig. 8) suggest low-sinuosity channels. The basal debrites (Figs. 5B and 5C) suggest an association with submarine landslide emplacement. The abundance of debrites within channel-fill and terrace deposits (Fig. 6) and the mapping from Bayliss and Pickering (2015) suggest that channel belts occupy a topographic low within the Aínsa depocentre. Channel-fill deposits (FA3) are thicker-bedded, more amalgamated, and up to 3 times thicker than the terrace deposits (FA2) (15m vs 5 m), suggesting that the terrace surfaces formed in elevated adjacent areas to the channel (Babonneau et al., 2002, 2004, 2010; Hansen et al., 2015, 2017a, 2017b). The nature of the channel-fill and terrace deposits will vary according to the magnitude of flows along the channel thalweg (Babonneau *et al.*, 2004; Dennielou *et al.*, 2006). Low-magnitude flows are likely to be fully confined within the channel thalweg, and only the upper and more dilute parts of the flow will deposit onto the terrace surfaces, producing fine-grained thin beds (Hansen *et al.*, 2015). In contrast, the lower and upper parts of high-magnitude flows will override the channel margin and terraces, with only the basal part of the flow confined to the channel belt (Babonneau et al., 2004; Hansen et al., 2015, 2017a). High-magnitude flows are likely to result in bypass/erosion within the main channel thalweg, partial bypass and tractional reworking on the terrace, and deposition on the overbank areas if they overspill (Peakall *et al.*, 2000; Kane *et al.*, 2007; Hubbard *et al.*, 2008; Kane & Hodgson, 2011; McArthur *et al.*, 2016; Hansen *et al.*, 2017a). Changes in flow magnitude through time will result in a high degree of variability in bed thicknesses and grain size in the terrace deposits, which are unlikely to be recorded in the channel axis. However, channel-fill deposits (FA3) lack major erosional surfaces (only minor scouring), indicating a more depositional phase than channel initiation, incision and bypass. Therefore, the channel-fill deposits recognized in the studied section are likely related to channel abandonment or backfilling (Morris and Normark, 2000; Hodgson et al., 2016).

Confined overbank

Confined overbank areas consist of three facies associations: overbank (FA1), crevasse scour-fill (FA4) and crevasse lobe (FA5) deposits (Fig. 6, 7 and 8), which are interpreted to represent depositional environments outside the channel belt. Overbank deposits are the most abundant facies association and include slumps and slides (Fig. 6). Crevasse scour-fills and crevasse lobes form a 14-metre thick crevasse complex (Fig. 9 and 10), interrupting the otherwise monotonous thin-bedded mudstone-dominated overbank deposition. The crevasse complex comprises i) a 4 m thick basal crevasse scour-fill, characterised by poor lateral continuity (FA4), overlain by ii) a 10 m thick thinning-upward laterally-continuous package, composed of 1.5 to 5 m thick and at least 1 km long aggradationally stacked crevasse lobes (Figs. 8, 9 and 10). Bed thickness and sandstone bed amalgamation decrease upward and laterally in the crevasse complex (Figs. 8 and 10). Crevasse lobes are bounded by centimetre-scale mudstone packages (Lf1) and decimetre-scale sheared mudstones (Lf7c). The sheared mudstone packages are only found within the crevasse complex (Fig. 6). The lowermost and thickest (up to 5 m) crevasse lobe onlaps onto the slide scar of the underlying slump towards the NE (across strike), with abrupt thinning rates (25 m/km; Figs. 7 and 8). However, the slumps are truncated by an SW-dipping surface, interpreted to represent the slide scar of a younger mass failure (Figs. 7 and 8). Thinning rates within the crevasse lobe complex are lower towards NW (downdip), where the medium- to thick-bedded sandstones gradually thin (1m/km) into thin-bedded sandstones over 1 km (Fig. 8). No bed pinch-out was documented along the downdip transect due to the tabularity of crevasse lobe thin beds (Fig. 8). Unlike the lowermost crevasse lobes, the uppermost thin-bedded crevasse lobes do not pass laterally into thick-bedded sandstones, instead showing a tabular architecture (Figs. 6 and 8). The term' confined overbank' is used here instead of external levees (Kane and Hodgson, 2011) because the tectonic setting of narrow foreland channel systems confined between two opposing slopes resulted in insufficient space to construct wedge-shaped levees. A comparable confinement scale has been documented in the Puchkirchen Formation in the Austrian Molasse Basin (overbank wedges of De Ruig and Hubbard, 2006; Hubbard et al., 2009; Kremer et al., 2018). Tectonically-active margins can also promote overbank asymmetry (Kane et al., 2010b; Hansen et al., 2017a; Kneller et al., 2020); therefore, such tectonic control is expected to result in an asymmetry between the northeastern and southwestern overbank deposits of the Banastón II sub-unit. However, given that the southwestern overbank area of the Banastón II sub-unit does not crop out in the study area, this asymmetry remains unproven.

DISCUSSION

Channel margin collapse and crevasse complex development

Fine-grained sedimentation in the confined overbank areas was interrupted by the deposition of anomalously thick sandstone beds related to the development of the crevasse complex. Crevasse complexes result from the breaching of the channel belt (Sawyer *et al.*, 2007, 2014), allowing (parts of) high-density turbidity currents to escape channel-belt confinement (Posamentier and Kolla, 2003; De Ruig and Hubbard, 2006; Hubbard et al., 2009; Armitage et al., 2012; Brunt et al., 2013; Maier et al., 2013; Morris et al., 2014a). The most commonly documented breaching mechanisms are enhanced bank erosion by downstream meander migration (sweep) and/or lateral meander growth (swing) (e.g. Peakall et al., 2000; Abreu et al., 2003; Deptuck et al., 2003) and mechanical weakening by overpressure leading to collapse of channel margins (e.g. Sawyer et al., 2014) or external levees (Ortiz-Karpf *et al.*, 2015). Given the low sinuosity of the Banastón channel, the onlap against a slide scar, and the juxtaposition of the crevasse complex over a slump, channel wall collapse into the channel belt is considered the most plausible mechanism for the initiation of the crevasse complex studied here.

The crevasse scour-fill facies association is interpreted as the most proximal environment of the crevasse complex. Localized acceleration of turbidity currents can produce incisions, promoting further erosion (Eggenhuisen *et al.*, 2011). The juxtaposition of crevasse lobes over crevasse scour-fills might represent a change from bypass to backfilling due to the shape of the slide scar, which is likely to be narrowest at the base and widens upwards. This morphology is likely to promote localized flow constriction (Kneller, 1995), resulting in accumulative (Kneller and Branney, 1995; Kneller and McCaffrey, 1999; Soutter et al., 2021), waxing (Kneller, 1995; Mulder and Alexander, 2001) and partially bypassing turbidity currents (Talling *et al.*, 2012; Stevenson *et al.*, 2015). Substrate excavation can promote local mass failures from slide scar walls, as demonstrated by the interfingering of sand-fill scours (Lf5) and sheared mudstone intervals (Lf7c). This phenomenon has been reported in kilometre-scale submarine landslides, where sidewall fragmentation promotes secondary mass failures and reshapes the original slide scar (Richardson *et al.*, 2011). This effect could increase the aspect ratio (width: height) of the breach, reducing flow constriction and promoting deposition. The upward thinning and fining with increasing tabularity of sandstone beds within the crevasse lobes suggests progressive filling of the accommodation in the confined overbank and/or the abandonment of the adjacent channel through avulsion or reduced sediment supply. Alternatively, it could represent a compensational stacking pattern of crevasse lobes, similar to the crevasse splays documented in fluvial systems (Donselaar *et al.*, 2013; van Toorenenburg *et al.*, 2016; Burns *et al.*, 2019) or in deep-water frontal lobes (Prélat *et al.*, 2009) and that the crevasse scour-fills and/or crevasse lobes are not associated with the same crevasse node.

We propose that the nature of the crevasse complex is controlled by the origin of the channel margin collapse scar and subsequent modification and healing, and its stratigraphic evolution reflects the re-establishment of the overbank area after the breach. Crevasse lobe development has also been observed in the subsurface Puchkirchen Formation in the Austrian Molasse Basin (De Ruig and Hubbard, 2006; Hubbard et al., 2009). However, the crevasse lobes in the Austrian Molasse Basin are not identified on the active margin of the channel system. In this study, the abundance of slides and slumps in the studied section (16.1% and 12.2% cumulative thickness, respectively) suggest that they played a key role in creating the conditions to develop crevasse lobes near the active margin. The thickest part of a slide (among other submarine landslides) is likely to be found in the lower compressional domain. In contrast, the upper, extensional domain of submarine landslides is thinner and might create accommodation towards the slide scar (Figs. 10 and 11A; Kremer et al., 2018; Ayckbourne et al., 2022). Breaching by the collapse of the channel margin would leave behind some concave topography in the overbank areas susceptible to being exploited as a conduit for subsequent flows (Damuth et al., 1988; Posamentier and Kolla, 2003; Fildani and Normark, 2004; Armitage et al., 2012; Brunt et al., 2013; Maier et al., 2013; Morris et al., 2014a; Ayckbourne et al., 2022). Slide and slump emplacement would also locally reduce the steepness of the active margin and, therefore, the 'valley-confinement'. Thus, flows can escape the channel belt more easily, spreading laterally to deposit sand on the otherwise mudstone-dominated overbank (Fig. 11). This study, therefore, highlights how small-scale submarine landslides (in this case < 10 m thick) and secondary mass failures can effectively induce crevasse lobe development on active margins and therefore provide a means of trapping sand on the slope.

The impact of submarine landslides on channelised flows and terraces

Submarine landslides are emplaced longitudinally (Bernhardt *et al.*, 2012; Masalimova *et al.*, 2015) and transversely (De Ruig and Hubbard, 2006; Hubbard et al., 2009; Kremer et al., 2018) in peripheral foreland basins. Despite the outcrop limitations and lack of kinematic indicators within the debrites (Bull *et al.*, 2009), the position and composition of submarine landslide deposits within the palaeogeography of the Banastón sub-unit suggests that they were emplaced transversely (Bayliss and Pickering, 2015) and probably related to tectonic pulses, given the tectonically-active nature of the basin and their abundance. Submarine landslides can disturb the slope equilibrium gradient (Corella *et al.*, 2016; Kremer *et al.*, 2018; Liang *et al.*, 2020; Tek *et al.*, 2020) and induce partial or full blockage of the adjacent conduit (Posamentier and Kolla, 2003; Bernhardt et al., 2012; Corella et al., 2016; Kremer et al., 2018; Tek et al., 2020; Tek et al., 2021; Allen et al., 2022).

Sediment gravity flows travelling over debrites can show complex patterns of flow behaviour and resultant deposit character due to the upper surface rugosity of the debrite, which promotes rapid deposition (and associated foundering) and/or erosion and channelisation (Armitage et al., 2009; Fairweather, 2014; Kneller et al., 2016; Valdez et al., 2019; Tek et al., 2020; Martínez-Doñate et al., 2021; Allen et al., 2022). Channelisation can create a positive feedback loop, with enhanced erosion in the channel further increasing confinement (Eggenhuisen *et al.*, 2011; De Leeuw *et al.*, 2016; Hodgson *et al.*, 2016), leading to the development of a conduit bounded laterally by elevated terraces (Hansen et al., 2017b; Tek et al., 2021), as suggested by the finning upward trend recorded in terrace deposits (FA2; Fig. 5B). Recent studies based on high-resolution bathymetry and shallow subsurface datasets (Tek et al., 2021) and field-based studies (Allen *et al.*, 2022) suggest that unplugging of the previously damming submarine landslides is more complex than previously thought due to the development of knickpoints that migrate upstream from downstream of the submarine landslide. The high degree of bed amalgamation and lack of metre-scale erosional surfaces in the investigated channel-fill deposits indicate high aggradation rates rather than bypassing sediment gravity flows. We interpret this stratal architecture as indicative of channel backfilling (Pickering *et al.*, 2001) due to damming induced by debrite emplacement or tectonically-controlled upstream avulsion due to thrust propagation, as observed in older channel systems within the Aínsa depocentre (Arro system; Millington and Clark, 1995; Tek et al., 2020). Therefore, it is suggested here that the emplacement of submarine landslides within the channel belt impacts channelised flows, and it is the primary mechanism for promoting terrace development in the Banastón II sub-unit.

Avulsion mechanism(s) in the Banastón II channel system

Long-lived breaching is common on the outer bends of sinuous channels confined by external levees in unconfined settings (Damuth et al., 1988; Posamentier and Kolla, 2003;

Fildani and Normark, 2004; Armitage et al., 2012; Brunt et al., 2013; Maier et al., 2013; Morris et al., 2014a) and provides an effective mechanism for the avulsion of the channel system, which might be preceded by the deposition of crevasse lobes (Damuth *et al.*, 1988; Armitage *et al.*, 2012; Brunt *et al.*, 2013; Ortiz-Karpf et al., 2015). However, crevasse lobe development in small, peripheral foreland basin settings is unlikely to lead to avulsion and re-routing of the entire channel belt (Flood *et al.*, 1991) due to low channel sinuosity and structural confinement (Hubbard *et al.*, 2009). The lack of avulsion and related cannibalization of the channel-belt fill, and the presence of a confined overbank on the active margin, explain why crevasse scours fills and lobes are preserved in the Banastón II system. It is unlikely that the emplacement of a few submarine landslides could drive the avulsion of the entire Banastón II deep-water channel system, given their small scale (< 10 m thick) compared to the scale of the channel system (98 m thick and 1800 m wide) and the structural confinement (~5-8 km wide syncline). Active tectonism in the foreland basin and related uplift and steepening of the active lateral margin likely triggered abundant mass failure events. The progressive uplift and south-westward advancement of the active margin possibly promoted the development of a series of transverse submarine landslides running parallel to the strike of the active margin (Fig. 11) that may have enhanced the SW-directed lateral migration of the channel belt (e.g. Posamentier and Kolla, 2003; Deptuck et al., 2007; Kane et al., 2010a; McHargue et al., 2011) as also suggested by Bayliss and Pickering (2015). Even if subsequent channelised sediment gravity flows are not fully ponded after submarine landslide emplacement, they are likely to undergo constriction (Kneller, 1995) and deflection away from the active margin, producing punctuated channel migration (*sensu* Maier et al., 2012) and breaching. Therefore, we propose that repeated emplacement of submarine landslides, related to the syn-depositional growth of local structures adjacent to channel belts, determined the channel architecture, the sites of crevasse complex deposits, playing a key role in the lateral offset of the Banastón system and storage of sand in the slope.

Conclusions

The stratigraphic evolution of the Banastón II sub-unit in the San Vicente area records the lateral offset of a submarine channel system, which we relate to the syn-depositional growth of local structures and related mass-wasting events. The active tectonism promoted submarine landslides, which impacted the dynamics of the channel system. The emplacement of debrites within channel belts resulted in channel damming and backfilling. Additionally, modification of the slope gradient caused by the emplacement of debrites was the main mechanism for terrace formation. The emplacement of slides and slumps raised the channel base and left concave-up evacuation scars in the confined overbank, which facilitated the formation of breach points exploited by subsequent flows to form a crevasse-scour and crevasse lobes. In contrast to previous studies in similar basin settings, we document this breaching mechanism towards the active margin instead of the passive margin. This study highlights that small-scale basin margin failures and their deposits can profoundly influence the dynamics of deep-water channels and their adjacent overbank areas on tectonically-confined submarine slopes.

Figures

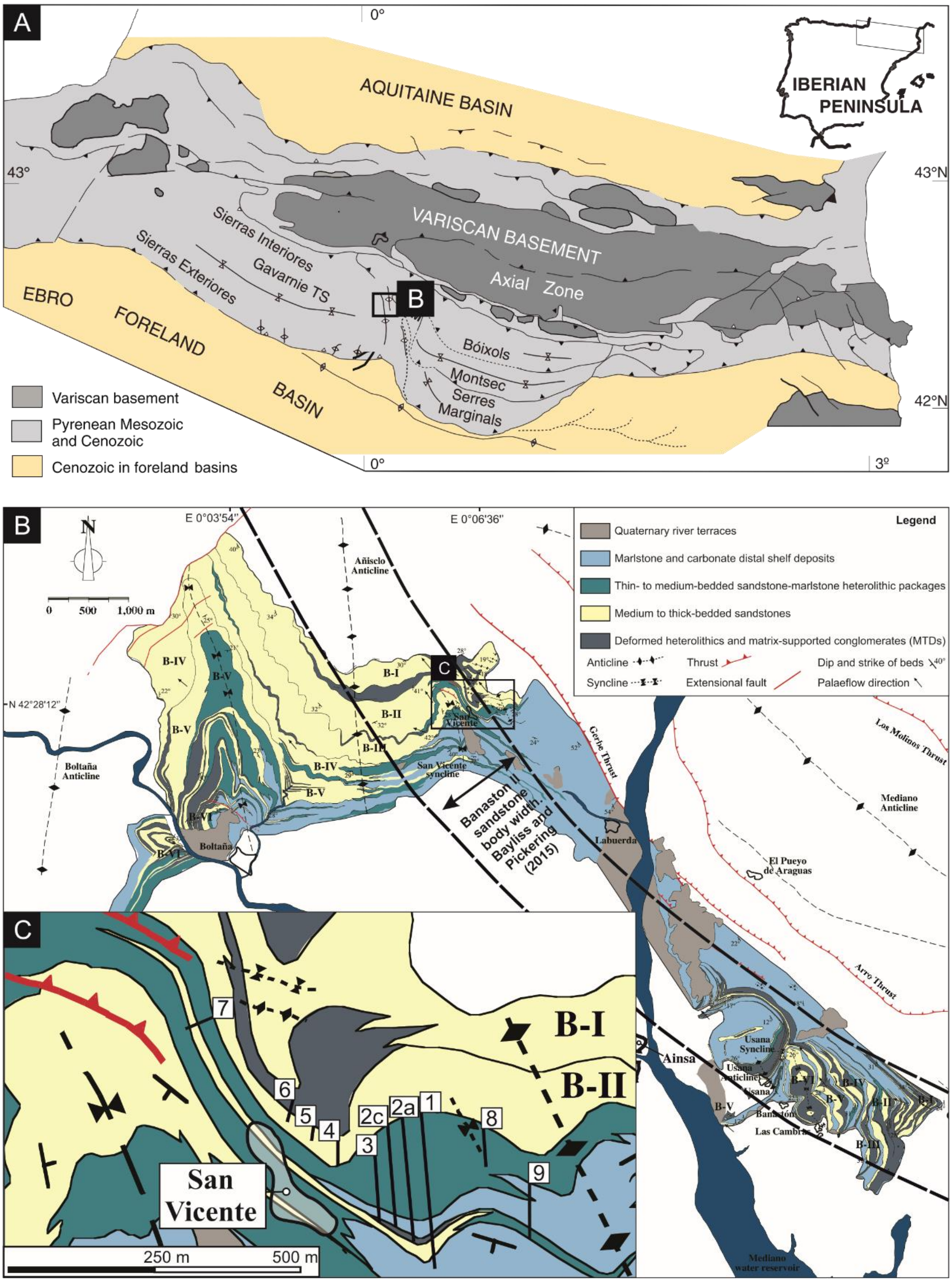

Fig. 1. (A) Structural map of the Pyrenees (after Muñoz et al., 2013) and location of the Aínsa Basin (See black square). (B) Geologic map of the Banastón system and the main structures (after Bayliss and Pickering, 2015). Note the black square indicating the location of the study area. (C) Geologic map of the study area near the San Vicente town

(after Pickering and Bayliss, 2009; Bayliss and Pickering, 2015) and the sedimentary logs collected in this study.

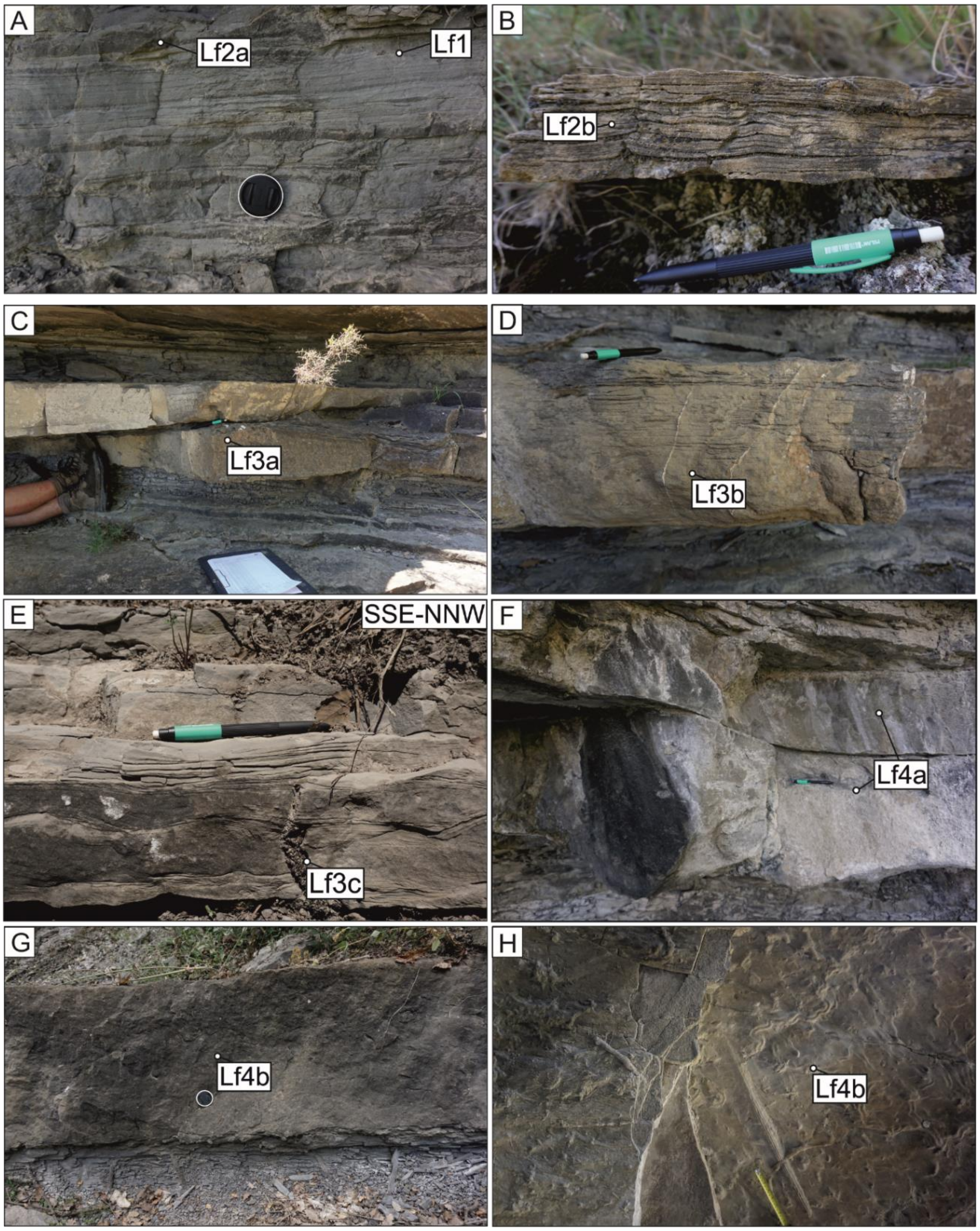

Fig. 1. Outcrop photographs of Lf1-Lf4b lithofacies. (A) Thin-bedded, fine-grained heterolithics characterised by the alternation between carbonate mudstone (Lf1) and Siltstone to fine-grained sandstones (Lf2a). (B) Thin-bedded planar-laminated sandstone (Lf2b). (C) Lenticular medium-bedded sandstones (Lf3a). Note the onlap of the sandstone

bed onto the Lf3a bed due to its positive relief. (D) Planar and ripple-laminated argillaceous medium-bedded sandstone (Lf3b). (E) Climbing-ripple medium-bedded sandstone (Lf3c). (F) Erosional mudstone clast-rich thick-bedded sandstones. Note pencil for scale. (G) Structureless thick-bedded argillaceous sandstones. (H) Base of structureless thick-bedded argillaceous sandstones with abundant bioturbation and groove marks.

Fig. 3. Outcrop photographs of Lf5 and Lf6 lithofacies. (A) Structureless and (B) dune-scale cross-bedded thick-bedded sandstone scour-fill. Note in (A) the abundant burrows at the scour dipping towards the right hand and in (B) the abundant mudstone clasts along the laminae. (C) Medium-bedded granular sandstone with well-developed NW migrating dune-like bedforms (Lf6). See the lens cap for scale. The cross-bedding is coarser-grained (granular to pebbly) than the surrounding sandstone (medium to very coarse). (D) Plan view of Lf6 showing the crescentic-shaped profiles. See geologist for scale. (E) Very coarse-grained sandstone bearing carbonate mudstone clasts. (F) Intensely bioturbated tops of Lf6.

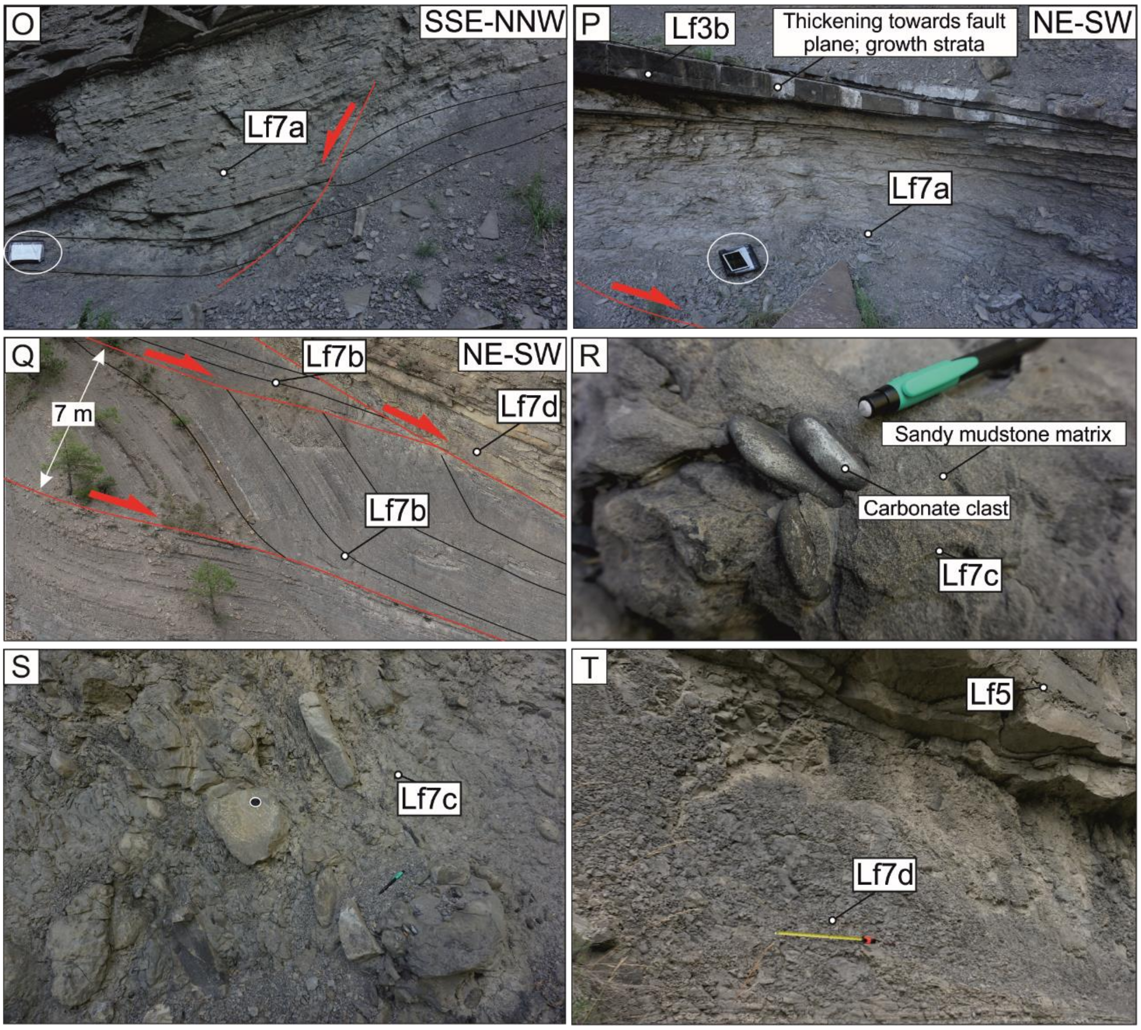

Fig. 4. Outcrop photographs of Lf7a-Lf7d lithofacies. (A) Rotated thin-bedded heterolithic package exhibits minor internal disaggregation (Lf7a) interpreted as slide deposits. The base of (Lf7a) is often marked by a concave-up glide plane. (B) At the top of Lf7a, < 0.3 m thick sandstone beds show localised thickening towards the slide plane and pinching away from it (towards the right hand). (C) Deformed heterolithic package characterised by metre-scale amplitude open to recumbent folding (Lf7b) interpreted as slump deposits. Normal faults and folds show SW vergence. (D and E) Matrix-supported poorly sorted and ungraded conglomerate (Lf7c) interpreted as debrites. Clasts show bimodal lithology: (C) sub-rounded carbonate clast (> 15 cm) and (E) sub-rounded to elongated sandstone clast (0.15 – 2 m). (F) Disaggregated and sheared carbonate mudstones, highly bioturbated (Lf7d), are interpreted as the deposits of the local failure of nearby fine-grained stratigraphy.

LITHOFACIES	LITHOLOGY	DESCRIPTION	THICKNESS	PROCESS INTERPRETATION	PHOTO
Lf1: Structureless mudstone	Carbonate mudstone	No gradation or structuration.	No clear bedding	Deposits from hemipelagic suspension fallout or low-density turbidity currents are too fine-grained to differentiate by the naked eye (Boulesteix *et al.*, 2019).	Fig. 2A
Lf2a: Lenticular thin-bedded siltstones and sandstones	Siltstone to fine-grained sandstones	Sandstones with flat bases and convex tops. Lenses can be 5-20 cm long.	1-10 cm	Deposition from a partially bypassing flow and reworking by distal, sluggish and small-volume low-density turbidity current (Allen, 1971, 1982; Jobe *et al.*, 2012).	Fig. 2A
Lf2b: Structured thin-bedded sandstones	Very fine to medium-grained sandstone	Normally graded, moderately-sorted thin-beds. Fine- to medium-grained bases and (very) fine-grained tops. Planar laminated from base to top.	1-10 cm	Deposition and tractional reworking by steady low-density turbidity current (Allen, 1971).	Fig. 2B
Lf3a: Lenticular medium-bedded sandstones	Very fine- to coarse-grained sandstones	Sandstones with flat bases and convex tops. Lenses can be 5-20 m long with 10-40 cm amplitudes. They are structureless at the base, overlain by planar or sinusoidal bedforms. Overlying deposits can onlap onto these sandstone bodies.	0-40 cm	Deposition from unsteady and unidirectional low- to medium-density turbidity currents (Allen, 1973; Kneller, 1995). Convex tops are associated with tractional reworking from bypassing and steady turbidity currents and/or deposition from combined flows (Tinterri, 2011) formed as a result of the interaction with intrabasinal topography (Pickering & Hiscott, 1985; Kneller *et al.*, 1991).	Fig. 2C
Lf3b: Planar laminated argillaceous medium-bedded sandstone	Coarse to fine-grained argillaceous sandstones	Argillaceous sandstones with well-developed planar laminations and wavy tops. The bed bases can be structureless.	10-60 cm	Deposits beneath mud-rich transitional plug flow are formed by steady, unidirectional and tractional reworking within the upper stage flow regime (Baas et al., 2009, 2011, Baas et al., 2016; Stevenson et al., 2020).	Fig. 2D
Lf3c: Climbing-ripple and sinusoidal laminated medium-	Coarse to fine-grained argillaceous sandstones	Bipartite sandstones comprise a sandy basal division passing gradually into the argillaceous division. Alternating structureless	10-50 cm.	Deposition from long-lived surging flows under high-aggradation rates and tractional reworking (Jobe *et al.*, 2012). The flows ultimately collapse, increasing the	Fig. 2E

bedded argillaceous sandstone		and supercritical climbing ripple lamination. Sinusoidal laminations are common near bed tops.		fallout rate and developing sinusoidal lamination (Tinterri, 2011; Jobe et al., 2012).	
Lf4a: Erosional mudstone clast-rich thick-bedded sandstones.	Coarse to fine-grained argillaceous sandstones	Highly amalgamated, crudely normally graded and structureless thick-bedded sandstones. Bed tops are silty, locally developing planar laminations towards bed tops. Bed bases are unconformable, with abundant grooves and bioturbation. Mudstone-clast-rich horizons and grain-size breaks are common.	0.5-1.2 m	Deposition under high-density partially bypassing turbidity currents (*sensu* Lowe, 1982), formed by incremental layer-by-layer deposition with high aggradation rates (Sumner *et al.*, 2008; Talling *et al.*, 2012). Scouring and entrainment of the fine-grained substrate are common.	Fig. 2F
Lf4b: Structureless thick-bedded argillaceous sandstones	Coarse to fine-grained argillaceous sandstones	Often amalgamated and structureless thick-bedded sandstones that become gradually argillaceous towards bed tops. Bed bases are mostly conformable; however, not always. Decimetre-scale burrows from top to basal contacts, not limited to bed bases.	0.5-1.2 m	Deposition from high-density turbidity currents (*sensu* Lowe, 1982) formed by incremental layer-by-layer deposition with high aggradation rates (Kneller and Branney, 1995; Sumner et al., 2008; Talling et al., 2012). The upper argillaceous division reflects the fine-grained tail of the flow, which collapsed due to radial spreading and abrupt loss in flow capacity.	Figs. 2G and 2H

Table 1. Description, process interpretation and photographs of the Lf1 – Lf4b lithofacies.

LITHOFACIES	LITHOLOGY	DESCRIPTION	THICKNESS	PROCESS INTERPRETATION	PHOTO
Lf5: Sand-filled scour	Argillaceous sandstone bearing abundant mudstone clasts along laminae	Medium- to thick-bedded sandstones with sharp unconformable concave-up (< 1 m) bases and flat tops. This lithofacies is structureless, planar laminated or dune-scale cross-bedded, bearing abundant mudstone clasts along laminae. Abundant burrows.	0.3-1 m	Deposition from high-density turbidity currents (*sensu* Lowe, 1982) formed by incremental layer-by-layer deposition with high aggradation rates (Kneller and Branney, 1995; Sumner et al., 2008; Talling et al., 2012). Planar and dune-scale cross-bedding bearing abundant mudstone clast along the laminae represent deposition from energetic, steady, and partially bypassing flows (Arnott, 2012; Talling *et al.*, 2012; Stevenson *et al.*, 2015).	FigA and Fig. 3B
Lf6: Medium-bedded granular sandstones	Medium to granular sandstone with mudstone clasts.	In plan view, medium-bedded granular sandstone with well-developed NW migrating dune-like bedforms with a crescentic shape. The cross-bedding is coarser-grained (granular to pebbly) than the surrounding sandstone (medium to very coarse). Rounded carbonate mudstone clasts are common.	20-50 cm	The abundant mudstone clasts suggest a partially bypassing flow (Stevenson *et al.*, 2015) that reworked the previously deposited coarse fraction, forming dunes. Dune-like bedforms are attributed to high-magnitude steady parental flow (Arnott, 2012; Talling *et al.*, 2012).	Figs. 3C, 3FigD, 3E and 3F.
Lf7a: Rotated heterolithics	Thin- to medium-bedded heterolithics.	Rotated heterolithic (Lf1, Lf2a, Lf2b) packages are characterised by decimetre-scale low-amplitude sinusoidal folding lacking internal disaggregation. Folding and normal faulting verge SW (perpendicular to palaeoflow and parallel to the SW dipping active margin). The base of the deposit is often marked by a concave-up	0.5-5 m	Local sliding of nearby stratigraphy (not disaggregated). Intraformational and non-erosional. The thickness changes of the top sandstone can be related to the pre-depositional rugosity of the slide (e.g. Armitage et al., 2009) or can be related to syn-depositional creeping/sliding (e.g. Ayckbourne et al., in press)	Figs. 4A and 4B

		glide plane. At the top of this package, < 0.3 m thick sandstone beds showing localised thickness changes are common; thickening in the hangingwall towards the fault when the Lf7a is thinnest and thinning or pinching out when Lf7a is thickest.			
Lf7b: Folded heterolithics	Thin- to thick-bedded heterolithics.	Deformed heterolithic (Lf1, Lf2a, Lf2b, Lf4a, Lf4b, Lf5, Lf6, Lf7c) package characterised by metre-scale amplitude open to recumbent folding. Normal faults and folds show SW vergence.	5-8 m	Local slumping of nearby stratigraphy (limited disaggregation). Intraformational and non-erosional. Equivalent to Type Ia MTCs of Pickering and Corregidor (2005).	Fig. 4C
Lf7c: Matrix-supported conglomerate	Mud-rich medium-grained sandstone to sandy mudstone.	Poorly sorted and ungraded with a chaotic distribution of clasts floating in a sandy mudstone matrix. Clasts show bimodal lithology: sub-rounded carbonate clast (> 15 cm) and sub-rounded to elongated sandstone clast (0.15 – 2 m). Irregular and sharp bases can be erosive, undulatory tops.	0.5-7 m	Cohesive debris-flow deposits (*sensu* Talling et al., 2012). The carbonate clasts are extraformational sediments eroded and reworked prior to their input to deep-water settings, while the sandstone clasts represent the rafting and incorporation of intraformational material into the debris flows. Equivalent to Type II MTCs of Pickering and Corregidor (2005).	Figs. 4D and 4E
Lf7d: Sheared mudstone	Carbonate mudstone	Disaggregated and sheared carbonate mudstones, highly bioturbated	0.1-3 m	Local failure of nearby fine-grained stratigraphy. Bioturbation suggests that these deposits were overridden by nutrient- and oxygen-bearing flows and proximity to channels.	Fig. 4F

Table 2. Description, process interpretation and photographs of the Lf5 and Lf6 and Lf7 lithofacies.

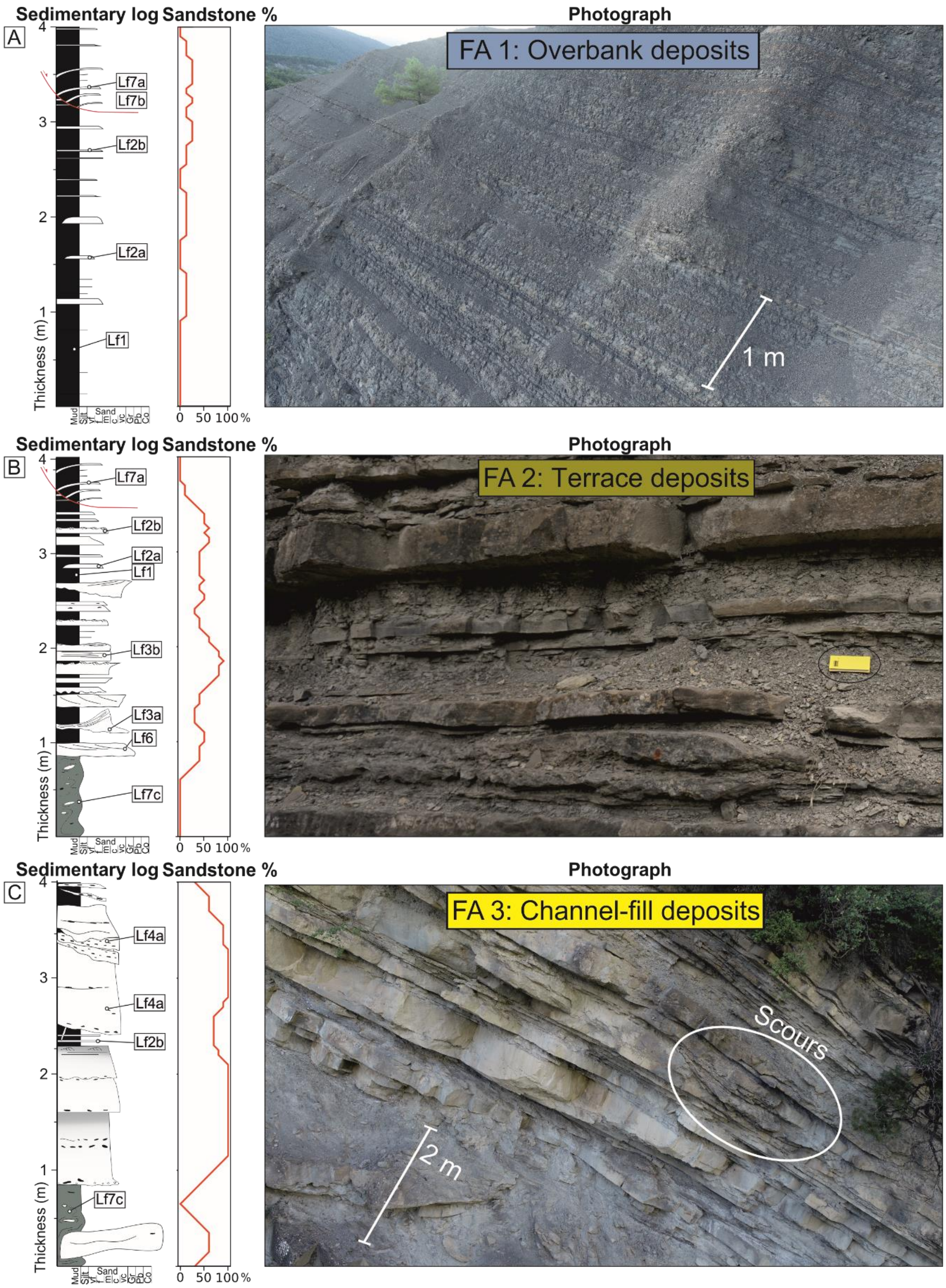
Sedimentary log
Sandstone %
Photograph
A
FA 1: Overbank deposits
Lf7a
Lf7b
Lf2b
Lf2a
Lf1
1 m
Thickness (m)
Mud
Silt
Sand
0
50
100 %
B
FA 2: Terrace deposits
Lf7a
Lf2b
Lf2a
Lf1
Lf3b
Lf3a
Lf6
Lf7c
C
FA 3: Channel-fill deposits
Lf4a
Lf4a
Lf2b
Lf7c
Scours
2 m

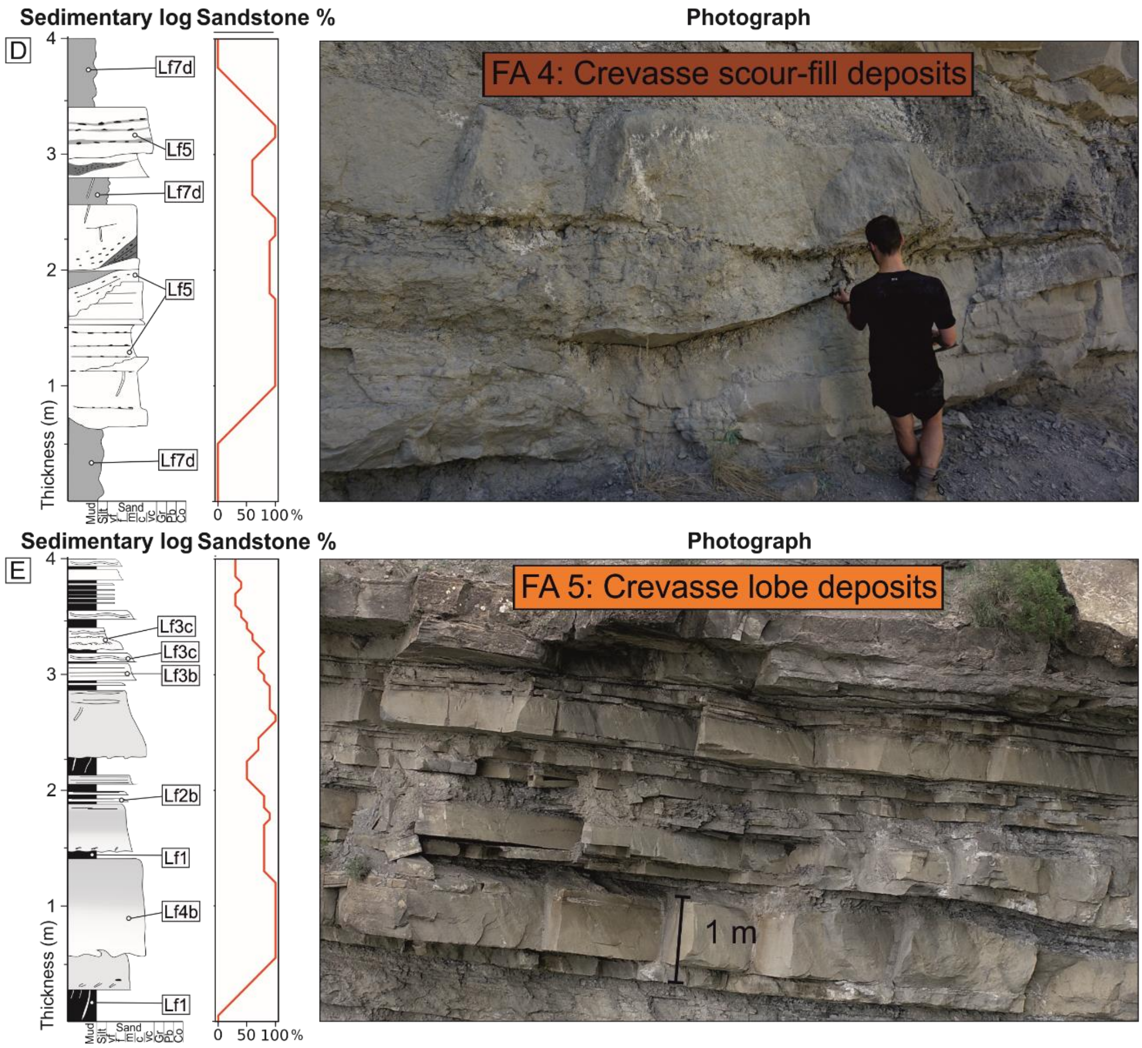

Fig. 5. Representative sedimentary log, sandstone proportion and photograph of the stratal packages representing facies associations (A) FA1: Overbank deposits, (B) FA2: Terrace deposits, (C) FA3: Channel-fill deposits, (D) FA4: Crevasse scour-fill deposits and (E) FA5: Crevasse lobes deposit.

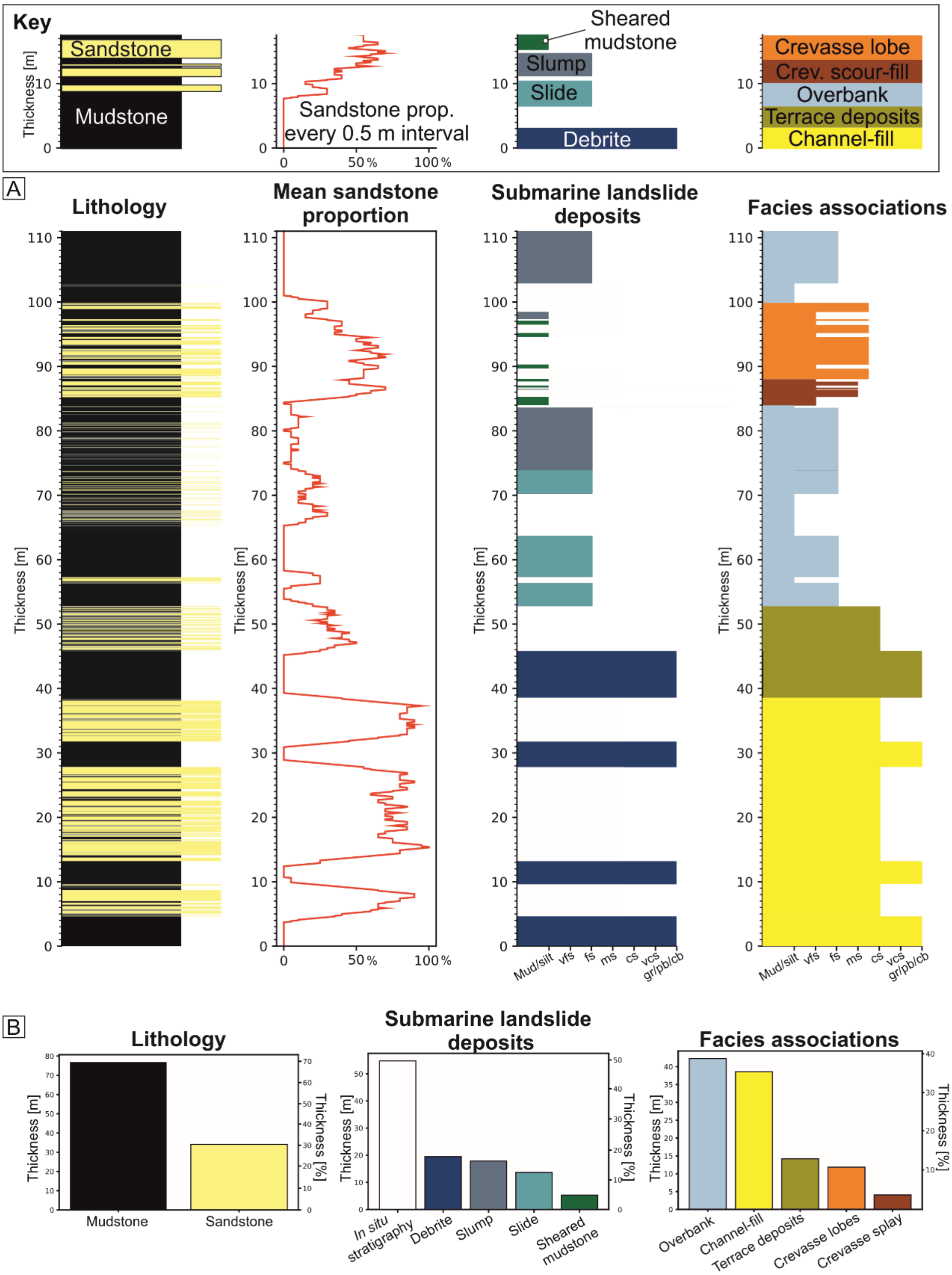

Fig. 6. A) Logs and (B) Histograms showing the lithology, mean sandstone proportion, submarine landslide content and facies associations of the 111 m thick study interval. The mean sandstone proportion is calculated using a moving average with a sample range of 0.5 m. The section is mudstone-dominated, especially on the upper half where the overbank facies association overlies channel-fill and terrace deposits. Note the variation of submarine landslide deposits along the section.

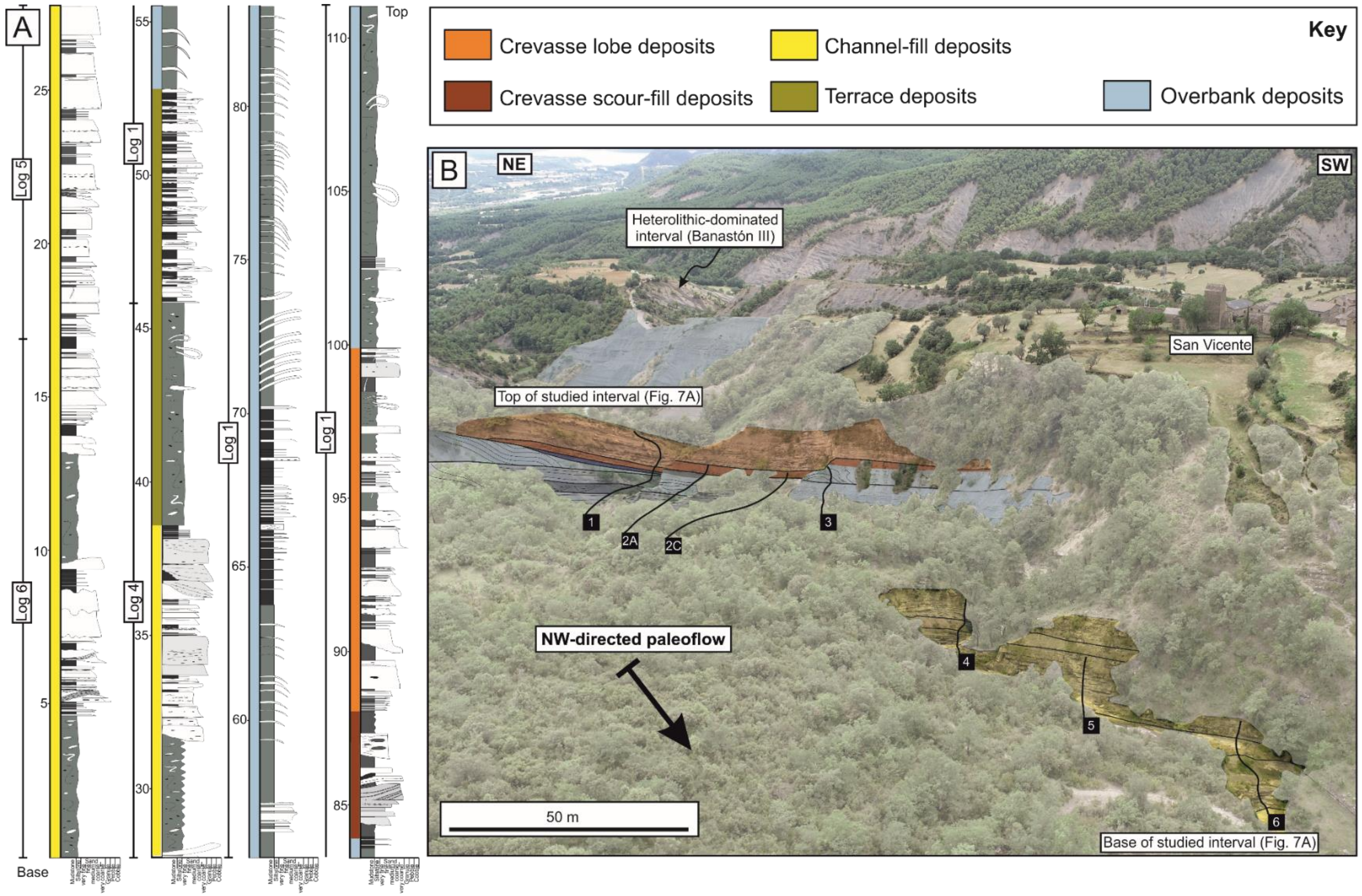

Fig 7 (A) Composite stratigraphic column of the investigated interval (111 m thick) of the Banastón II member and the different facies associations. (B) Interpreted UAV photographs with the different facies associations and sedimentary logs. Note the San Vicente town in the top right corner.

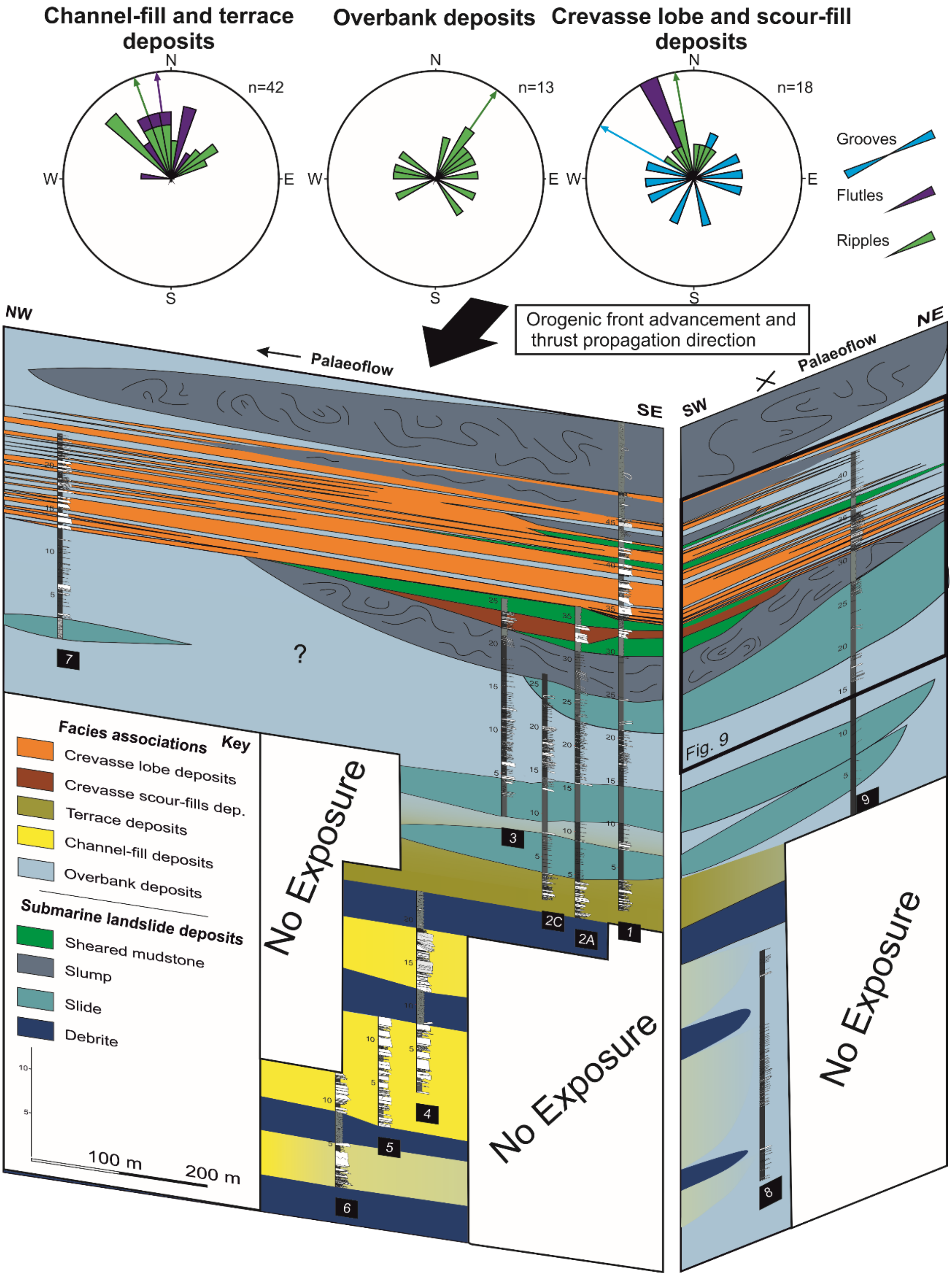

Fig. 8. Correlation panel of the Banastón II member near the San Vicente town. See Fig. 1**¡Error! No se encuentra el origen de la referencia.**C and 7B for the location of the sedimentary logs. Note from rose diagrams of the palaeocurrents that the overbank directions are more northwards than the channel belt and crevasse deposits.

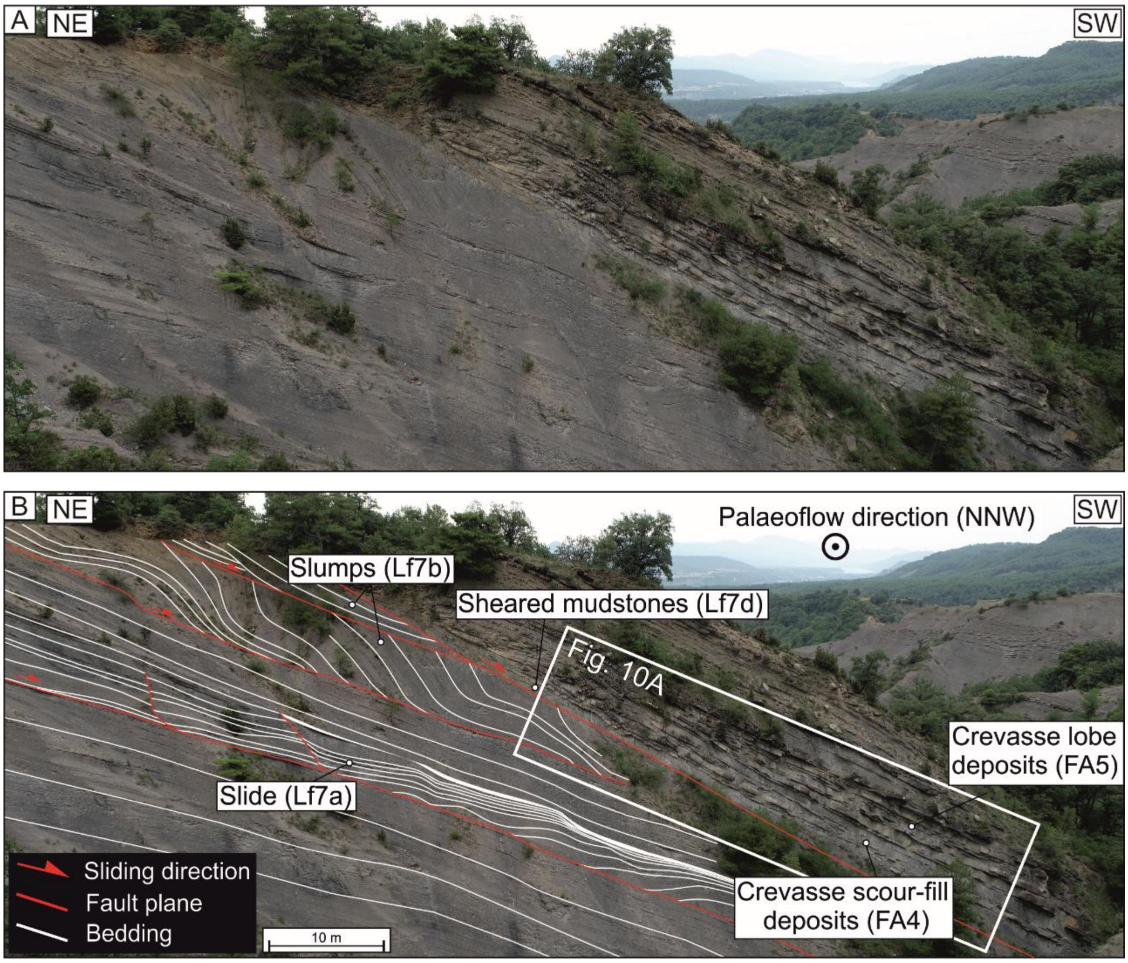

Fig. 9. (A) Uninterpreted and (B) interpreted UAV photographs of the multiple submarine landslides found within the overbank (FA1) and the crevasse scour-fills (FA4) and crevasse lobes deposits (FA5).

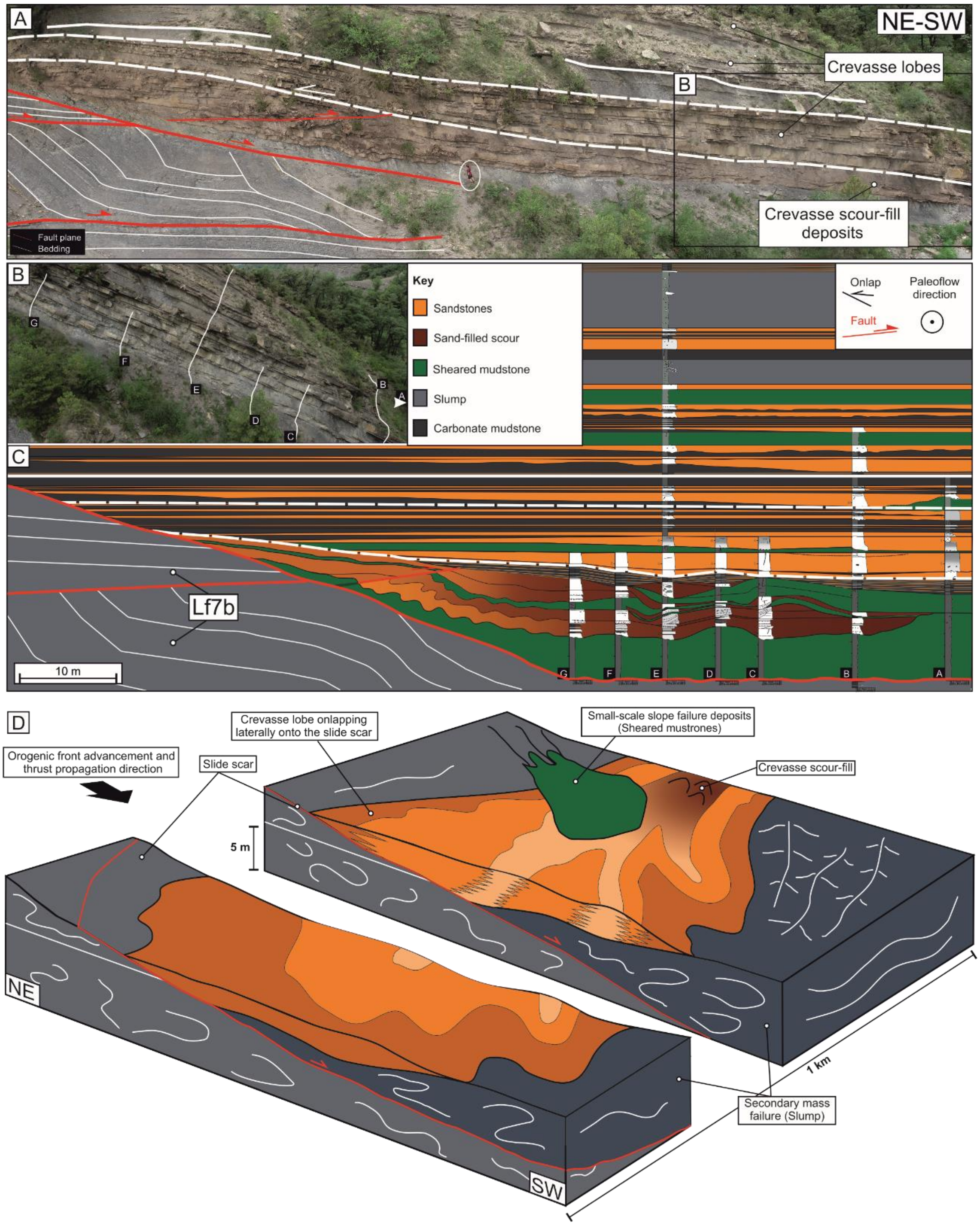

Fig. 10. (A) Interpreted UAV photograph showing a basal slide overlain by the crevasse complex. (B) Location of the sedimentary logs of the crevasse complex. (C) Correlation panel of a crevasse complex showing the juxtaposition of crevasse lobes over the basal crevasse scour-fill deposits. D) Model illustrating the crevasse lobe juxtaposed over a slump and laterally onlapping the slide scar.

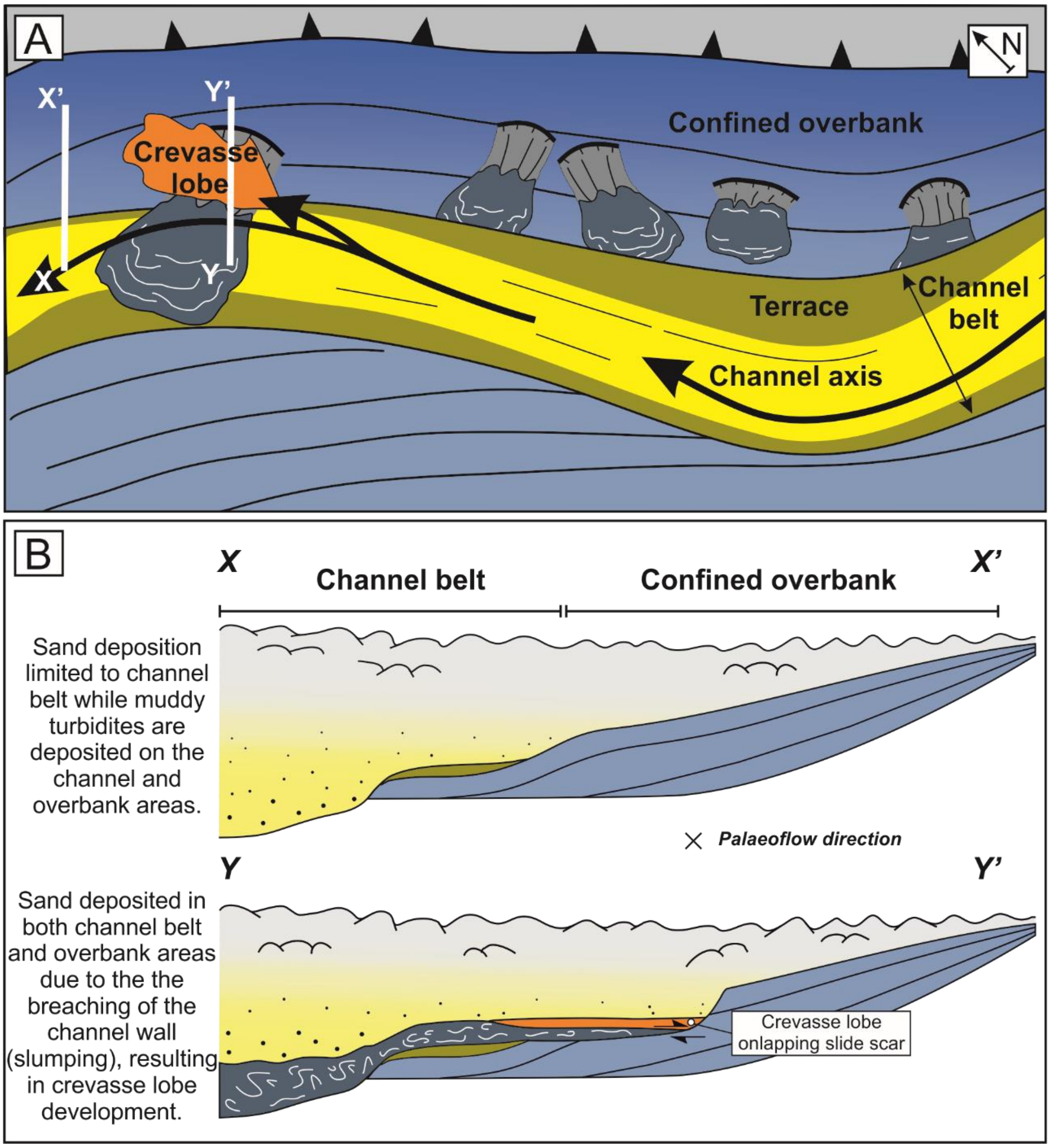

Fig. 11. (A) Evolutionary model illustrating the crevasse lobe deposition on the active margin due to submarine landslide emplacement, deflecting channelised flows towards the slide scar and (B) how the continuous transversely-sourced submarine landsliding is a potential mechanism of avulsion of the Banastón II member.

References

Abreu, V., **Sullivan, M.**, **Pirmez, C.** and **Mohrig, D.** (2003) Lateral accretion packages (LAPs): An important reservoir element in deep water sinuous channels. *Mar. Pet. Geol.*, **20**, 631–648.

Allen, C., **Gomis-Cartesio, L.E.**, **Hodgson, D.M.**, **Peakall, J.** and **Milana, J.P.** (2022) Channel incision into a submarine landslide on a Carboniferous basin margin, San Juan, Argentina: Evidence for the role of knickpoints.

Allen, J.R.L. (1971) Instantaneous sediment deposition rates deduced from climbing-ripple cross-lamination. *J. Geol. Soc. London.*, **127**, 553–561.

Allen, J.R.L. (1973) Phase differences between bed configuration and flow in natural environments, and their geological relevance. *Sedimentology*, **20**, 323–329.

Allen, J.R.L. (1982) Sedimentary structures, their character and physical basis Volume 1. Elsevier. 663 pp.

Amy, L., **Kneller, B.** and **McCaffrey, W.** (2000) Evaluating the Links Between Turbidite Characteristics and Gross System Architecture: Upscaling Insights from the Turbidite Sheet-System of Peïra Cava, SE France. *Deep. Reserv. World 20th Annu.*, 1–15.

Arbués, P., **Mellere, D.**, **Falivene, O.**, **Fernández, O.**, **Muñoz, J.A.**, **Marzo, M.** and **Gibert, J.M. De** (2007) Context and Architecture of the Ainsa-1-Quarry Channel Complex, Spain. *Atlas Deep. outcrops*, 1–20.

Armitage, D.A., **McHargue, T.**, **Fildani, A.** and **Graham, S.A.** (2012) Postavulsion channel evolution: Niger Delta continental slope. *Am. Assoc. Pet. Geol. Bull.*, **96**, 823–843.

Armitage, D.A., **Romans, B.W.**, **Covault, J.A.** and **Graham, S.A.** (2009) The Influence of Mass-Transport-Deposit Surface Topography on the Evolution of Turbidite Architecture: The Sierra Contreras, Tres Pasos Formation (Cretaceous), Southern Chile. *J. Sediment. Res.*, **79**, 287–301.

Arnott, R.W.C. (2012) Turbidites, and the case of the missing dunes. *J. Sediment. Res.*, **82**, 379–384.

Arnott, R.W.C. and **Al-Mufti, O.** (2017) Deep-marine pseudo dune cross-stratification-similar, but completely different. *J. Sediment. Res.*, **87**, 312–323.

Ayckbourne, A.J.M., **Jerrett, R.M.**, **Poyatos-Moré, M.**, **Watkinson, M.P.**, **Kane, I.A.** and **Taylor, K.G.** (2022) The Influence of creeping MTD topography on turbidity currents and their deposits: Examples from the Aínsa Basin (Spain).

Baas, J.H., **Best, J.L.** and **Peakall, J.** (2011) Depositional processes, bedform development and hybrid bed formation in rapidly decelerated cohesive (mud-sand) sediment flows. *Sedimentology*, **58**, 1953–1987.

Baas, J.H., **Best, J.L.** and **Peakall, J.** (2016) Comparing the transitional behaviour of kaolinite and bentonite suspension flows. *Earth Surf. Process. Landforms*, **41**, 1911–1921.

Baas, J.H., **Best, J.L.**, **Peakall, J.** and **Wang, M.** (2009) A phase diagram for turbulent, transitional, and laminar clay suspension flows. *J. Sediment. Res.*, **79**, 162–183.

Babonneau, N., **Cremer, M.** and **Bez, M.** (2010) Sedimentary architecture in meanders of a submarine channel: Detailed study of the present congo turbidite channel (zaiango project). *J. Sediment. Res.*, **80**, 852–866.

Babonneau, N., **Savoye, B.**, **Cremer, M.** and **Bez, M.** (2004) Multiple terraces within the deep incised Zaire Valley (ZaïAngo Project): Are they confined levees? *Geol. Soc. Spec. Publ.*, **222**, 91–114.

Babonneau, N., **Savoye, B.**, **Cremer, M.** and **Klein, B.** (2002) Morphology and architecture of the present canyon and channel system of the Zaire deep-sea fan. *Mar. Pet. Geol.*, **19**, 445–467.

Barnolas, A. and **Gil-Peña, I.** (2002) Ejemplos de relleno sedimentario multiepisódico en una cuenca de antepaís fragmentada: La Cuenca Surpirenaica. *Bol. Geol. y Min.*, **112**, 17–38.

Bayliss, N. and **Pickering, K.T.** (2015) Transition from deep-marine lower-slope erosional channels to proximal basin-floor stacked channel-levée-overbank deposits, and syn-sedimentary growth structures, Middle Eocene Banastón System, Ainsa Basin, Spanish Pyrenees. *Earth-Science Rev.*, **144**, 23–46.

Beaubouef, R.T. (2004) Deep-water leveed-channel complexes of the Cerro Toro Formation, Upper Cretaceous, southern Chile. *Am. Assoc. Pet. Geol. Bull.*, **88**, 1471–1500.

Beaubouef, R.T. and **Friedmann, S.J.** (2000) High Resolution Seismic/Sequence Stratigraphic Framework for the Evolution of Pleistocene Intra Slope Basins, Western Gulf of Mexico: Depositional Models and Reservoir Analogs. *Deep. Reserv. World 20th Annu.*, 40–60.

Bell, D., **Kane, I.A.**, **Pontén, A.S.M.**, **Flint, S.S.**, **Hodgson, D.M.** and **Barrett, B.J.** (2018) Spatial variability in depositional reservoir quality of deep-water channel-fill and lobe deposits. *Mar. Pet. Geol.*, **98**, 97–115.

Bernhardt, A., **Stright, L.** and **Lowe, D.R.** (2012) Channelized debris-flow deposits and their impact on turbidity currents: The Puchkirchen axial channel belt in the Austrian Molasse Basin. *Sedimentology,* **59**, 2042–2070.

Boulesteix, K., **Poyatos-Moré, M.**, **Flint, S.S.**, **Hodgson, D.M.**, **Taylor, K.T.** and **Brunt, R.L.** (2022) Sedimentologic and stratigraphic criteria to distinguish between basin-floor and slope mudstones: Implications for the delivery of mud to deep-water environments. *Depos. Rec.*, **8**, 958–988.

Boulesteix, K., **Poyatos-Moré, M.**, **Flint, S.S.**, **Taylor, K.G.**, **Hodgson, D.M.** and **Hasiotis, S.T.** (2019) Transport and deposition of mud in deep-water environments: Processes and stratigraphic implications. *Sedimentology*, **66**, 2894–2925.

Boulesteix, K., **Poyatos-Moré, M.**, **Hodgson, D.M.**, **Flint, S.S.** and **Taylor, K.G.** (2020) Fringe or background: Characterizing deep-water mudstones beyond the basinfloor fan sandstone pinchout. *J. Sediment. Res.*, **90**, 1678–1705.

Brunt, R.L., **Hodgson, D.M.**, **Flint, S.S.**, **Pringle, J.K.**, **Di Celma, C.**, **Prélat, A.** and **Grecula, M.** (2013) Confined to unconfined: Anatomy of a base of slope succession, Karoo Basin, South Africa. *Mar. Pet. Geol.*, **41**, 206–221.

Buffington, E.C. (1952) Submarine "Natural Levees". *J. Geol.*, **60**, 473–479.

Bull, S., **Cartwright, J.** and **Huuse, M.** (2009) A review of kinematic indicators from mass-transport complexes using 3D seismic data. *Mar. Pet. Geol.*, **26**, 1132–1151.

Burbank, D.W., **Puigdefabregas, C.** and **Anton Munoz, J.** (1992) The chronology of the Eocene tectonic and stratigraphic development of the eastern Pyrenean foreland basin, northeast Spain. *Geol. Soc. Am. Bull.*, **104**, 1101–1120.

Burns, C.E., **Mountney, N.P.**, **Hodgson, D.M.** and **Colombera, L.** (2019)

Stratigraphic architecture and hierarchy of fluvial overbank splay deposits. 629–649 pp.

Caja, M.A., **Marfil, R.**, **Garcia, D.**, **Remacha, E.**, **Morad, S.**, **Mansurbeg, H.**, **Amorosi, A.**, **Martínez-Calvo, C.** and **Lahoz-Beltrá, R.** (2010) Provenance of siliciclastic and hybrid turbiditic arenites of the Eocene Hecho Group, Spanish Pyrenees: Implications for the tectonic evolution of a foreland basin. *Basin Res.*, **22**, 157–180.

Canals, M., **Casamor, J.L.**, **Urgeles, R.**, **Lastras, G.**, **Calafat, A.M.**, **Masson, D.G.**, **Berné, S.** and **Alonso, B.** (2000) The Ebro Continental Margin, Western Mediterranean Sea: Interplay Between Canyon-Channel Systems and Mass Wasting Processes. *Deep. Reserv. World 20th Annu.*, 152–174.

Cantalejo, B. and **Pickering, K.T.** (2014) Climate forcing of fine-grained deep-marine systems in an active tectonic setting: Middle Eocene, Ainsa Basin, Spanish Pyrenees. *Palaeogeogr. Palaeoclimatol. Palaeoecol.*, **410**, 351–371.

Castelltort, S., **Honegger, L.**, **Adatte, T.**, **Clark, J.D.**, **Puigdefàbregas, C.**, **Spangenberg, J.E.**, **Dykstra, M.L.** and **Fildani, A.** (2017) Detecting eustatic and tectonic signals with carbon isotopes in deep-marine strata, Eocene Ainsa Basin, Spanish Pyrenees. *Geology*, **45**, 707–710.

Chanvry, E., **Deschamps, R.**, **Joseph, P.**, **Puigdefàbregas, C.**, **Poyatos-Moré, M.**, **Serra-Kiel, J.**, **Garcia, D.** and **Teinturier, S.** (2018) The influence of intrabasinal tectonics in the stratigraphic evolution of piggyback basin fills: Towards a model from the Tremp-Graus-Ainsa Basin (South-Pyrenean Zone, Spain). *Sediment. Geol.*, **377**, 34–62.

Clark, I.R. and **Cartwright, J.A.** (2011) Key controls on submarine channel development in structurally active settings. *Mar. Pet. Geol.*, **28**, 1333–1349.

Clark, J., **Puigdefàbregas, C.**, **Castelltort, S.** and **Fildani, A.** (2017) Propagation of Environmental Signals Within Source-to-sink Stratigraphy. In: *Spanish Pyrenees, June 5th-9th, 2017. SEPM (Society for Sedimentary Geology).*,

Corella, J.P., **Loizeau, J.L.**, **le Dantec, N.**, **Hilbe, M.**, **Gerard, J.**, **le Dantec, N.**, **Stark, N.**, **González-Quijano, M.** and **Girardclos, S.** (2016) The role of mass-transport deposits and turbidites in shaping modern lacustrine deepwater channels. *Mar. Pet. Geol.*, **77**, 515–525.

Curray, J.R., **Emmel, F.J.** and **Moore, D.G.** (2002) The Bengal Fan: Morphology, geometry, stratigraphy, history and processes. *Mar. Pet. Geol.*, **19**, 1191–1223.

Dakin, N., **Pickering, K.T.**, **Mohrig, D.** and **Bayliss, N.J.** (2013) Channel-like features created by erosive submarine debris flows: Field evidence from the Middle Eocene Ainsa Basin, Spanish Pyrenees. *Mar. Pet. Geol.*, **41**, 62–71.

Damuth, J.E., **Flood, R.D.**, **Kowsmann, R.O.**, **Belderson, R.H.** and **Gorini, M.A.** (1988) Anatomy and growth pattern of Amazon deep-sea fan as revealed by long-range side-scan sonar (GLORIA) and high-resolution seismic studies. *Am. Assoc. Pet. Geol. Bull.*, **72**, 885–911.

De Leeuw, J., **Eggenhuisen, J.T.** and **Cartigny, M.J.B.** (2016) Morphodynamics of submarine channel inception revealed by new experimental approach. *Nat. Commun.*, **7**, 1–7.

De Ruig, M.J. and **Hubbard, S.M.** (2006) Seismic facies and reservoir characteristics of a deep-marine channel belt in the Molasse foreland basin, Puchkirchen Formation, Austria. *Am. Assoc. Pet. Geol. Bull.*, **90**, 735–752.

Dennielou, B., **Huchon, A.**, **Beaudouin, C.** and **Berné, S.** (2006) Vertical grain-size variability within a turbidite levee: Autocyclicity or allocyclicity? A case study from the Rhône neofan, Gulf of Lions, Western Mediterranean. *Mar. Geol.*, **234**, 191–213.

Deptuck, M.E., **Steffens, G.S.**, **Barton, M.** and **Pirmez, C.** (2003) Architecture and evolution of upper fan channel-belts on the Niger Delta slope and in the Arabian Sea. *Mar. Pet. Geol.*, **20**, 649–676.

Deptuck, M.E., **Sylvester, Z.**, **Pirmez, C.** and **O'Byrne, C.** (2007) Migration-aggradation history and 3-D seismic geomorphology of submarine channels in the Pleistocene Benin-major Canyon, western Niger Delta slope. *Mar. Pet. Geol.*, **24**, 406–433.

Donselaar, M.E., **Cuevas Gozalo, M.C.** and **Moyano, S.** (2013) Avulsion processes at the terminus of low-gradient semi-arid fluvial systems: Lessons from the Río Colorado, Altiplano endorheic basin, Bolivia. *Sediment. Geol.*, **283**, 1–14.

Dreyer, T., **Corregidor, J.**, **Arbues, P.** and **Puigdefabregas, C.** (1999) Architecture of the tectonically influenced Sobrarbe deltaic complex in the Ainsa Basin, northern Spain. *Sediment. Geol.*, **127**, 127–169.

Eggenhuisen, J.T., **Mccaffrey, W.D.**, **Haughton, P.D.W.** and **Butler, R.W.H.** (2011) Shallow erosion beneath turbidity currents and its impact on the architectural development of turbidite sheet systems. *Sedimentology*, **58**, 936–959.

Fairweather, L. (2014) Mechanisms of supra MTD topography generation and the interaction of turbidity currents with such deposits. *PhD Thesis*, **1**, 242.

Fernández, O., **Muñoz, J.A.**, **Arbués, P.** and **Falivene, O.** (2012) 3D structure and evolution of an oblique system of relaying folds: The Ainsa basin (Spanish Pyrenees). *J. Geol. Soc. London.*, **169**, 545–559.

Fildani, A. and **Normark, W.R.** (2004) Late Quaternary evolution of channel and lobe complexes of Monterey Fan. *Mar. Geol.*, **206**, 199–223.

Flood, R.D., **Manley, P.L.**, **Kowsmann, R.O.**, **Appi, C.J.** and **Pirmez, C.** (1991) Seismic facies and late Quaternary growth of Amazon submarine fan. In: *Seismic facies and sedimentary processes of submarine fans and turbidite systems, Springer*, New York, 415–433.

Fontana, D., **Zuffa, G.G.** and **Garzanti, E.** (1989) The interaction of eustacy and tectonism from provenance studies of the Eocene Hecho Group Turbidite Complex (south-central Pyrenees, Spain). *Basin Res.*, **2**, 223–237.

Gee, M.J.R. and **Gawthorpe, R.L.** (2006) Submarine channels controlled by salt tectonics: Examples from 3D seismic data offshore Angola. *Mar. Pet. Geol.*, **23**, 443–458.

Georgiopoulou, A. and **Cartwright, J.A.** (2013) A critical test of the concept of submarine equilibrium profile. *Mar. Pet. Geol.*, **41**, 35–47.

Gupta, K. Das and **Pickering, K.T.** (2008) Petrography and temporal changes in petrofacies of deep-marine Ainsa-Jaca basin sandstone systems, Early and Middle Eocene, Spanish Pyrenees. *Sedimentology*, **55**, 1083–1114.

Hampton, M.A., **Lee, H.J.** and **Locat., J.** (1995) Submarine Landslides. *Rev. Geophys.*, **34**, 33-59.

Hansen, L.A.S., **Callow, R.**, **Kane, I.A.** and **Kneller, B.** (2017a) Differentiating submarine channel-related thin-bedded turbidite facies: Outcrop examples from the

Rosario Formation, Mexico. *Sediment. Geol.*, **358**, 19–34.

Hansen, L.A.S., **Callow, R.H.T.**, **Kane, I.A.**, **Gamberi, F.**, **Rovere, M.**, **Cronin, B.T.** and **Kneller, B.C.** (2015) Genesis and character of thin-bedded turbidites associated with submarine channels. *Mar. Pet. Geol.*, **67**, 852–879.

Hansen, L.A.S., **Hodgson, D.M.**, **Pontén, A.**, **Thrana, C.** and **Obradors Latre, A.** (2021) Mixed axial and transverse deep-water systems: The Cretaceous post-rift Lysing Formation, offshore Norway. *Basin Res.*, 1–23.

Hansen, L.A.S., **Janocko, M.**, **Kane, I.** and **Kneller, B.** (2017b) Submarine channel evolution, terrace development, and preservation of intra-channel thin-bedded turbidites: Mahin and Avon channels, offshore Nigeria. *Mar. Geol.*, **383**, 146–167.

Heezen, B.C., **Ewing, M.** and **Menzies, R.J.** (1955) The Influence of Submarine Turbidity Currents on Abyssal Productivity. *Oikos*, **6**, 170–182.

Heiniö, P. and **Davies, R.J.** (2007) Knickpoint migration in submarine channels in response to fold growth, western Niger Delta. *Mar. Pet. Geol.*, **24**, 434–449.

Hiscott, R.N. (1994) Loss of capacity, not competence, as the fundamental process governing deposition from turbidity currents. *J. Sediment. Res.*, **64**, 209–214.

Hodgson, D.M., **Kane, I.A.**, **Flint, S.S.**, **Brunt, R.L.** and **Ortiz-Karpf, A.** (2016) Time-transgressive confinement on the slope and the progradation of basin-floor fans: Implications for the sequence stratigraphy of deep-water deposits. *J. Sediment. Res.*, **86**, 73–86.

Hofstra, M., **Peakall, J.**, **Hodgson, D.M.** and **Stevenson, C.J.** (2018) Architecture and morphodynamics of subcritical sediment waves in an ancient channel–lobe transition zone. *Sedimentology*, **65**, 2339–2367.

Hubbard, S.M., **de Ruig, M.J.** and **Graham, S.A.** (2009) Confined channel-levee complex development in an elongate depo-center: Deep-water Tertiary strata of the Austrian Molasse basin. *Mar. Pet. Geol.*, **26**, 85–112.

Hubbard, S.M., **Jobe, Z.R.**, **Romans, B.W.**, **Covault, J.A.**, **Sylvester, Z.** and **Fildani, A.** (2020) The stratigraphic evolution of a submarine channel: linking seafloor dynamics to depositional products. *J. Sediment. Res.*, **90**, 673–686.

Hubbard, S.M., **Romans, B.W.** and **Graham, S.A.** (2008) Deep-water foreland basin deposits of the Cerro Toro Formation, Magallanes basin, Chile: Architectural elements of a sinuous basin axial channel belt. *Sedimentology*, **55**, 1333–1359.

Hübscher, C., **Spieß, V.**, **Breitzke, M.** and **Weber, M.E.** (1997) The youngest channel-levee system of the Bengal Fan: Results from digital sediment echosounder data. *Mar. Geol.*, **141**, 125–145.

Jobe, Z.R., **Lowe, D.R.** and **Morris, W.R.** (2012) Climbing-ripple successions in turbidite systems : depositional environments , sedimentation rates and accumulation times. 867–898.

Kane, I.A., **Catterall, V.**, **McCaffrey, W.D.** and **Martinsen, O.J.** (2010a) Submarine channel response to intrabasinal tectonics: The influence of lateral tilt. *Am. Assoc. Pet. Geol. Bull.*, **94**, 189–219.

Kane, I.A. and **Clare, M.A.** (2019) Dispersion, accumulation, and the ultimate fate of microplastics in deep-marine environments: A review and future directions. Front Earth Sci. doi: 10.3389/feart.2019.00080

Kane, I.A. and **Hodgson, D.M.** (2011) Sedimentological criteria to differentiate submarine channel levee subenvironments: Exhumed examples from the Rosario

Fm. (Upper Cretaceous) of Baja California, Mexico, and the Fort Brown Fm. (Permian), Karoo Basin, S. Africa. *Mar. Pet. Geol.*, **28**, 807–823.

Kane, I.A., **Kneller, B.C.**, **Dykstra, M.**, **Kassem, A.** and **McCaffrey, W.D.** (2007) Anatomy of a submarine channel-levee: An example from Upper Cretaceous slope sediments, Rosario Formation, Baja California, Mexico. *Mar. Pet. Geol.*, **24**, 540–563.

Kane, I.A., **McCaffrey, W.D.** and **Martinsen, O.J.** (2009) Allogenic vs. autogenic controls on megaflute formation. *J. Sediment. Res.*, **79**, 643–651.

Kane, I.A., **McCaffrey, W.D.**, **Peakall, J.** and **Kneller, B.C.** (2010b) Submarine channel levee shape and sediment waves from physical experiments. *Sediment. Geol.*, **223**, 75–85.

Kane, I.A., **McGee, T.D.**, **Jobe, Z.R.**, **Alsop, G.I.**, **Archer, S.G.**, **Hartley, A.J.**, **...** and **Hodgkinson, R.** (2012) Halokinetic effects on slope equilibrium profiles: Submarine channel evolution and implications for facies architecture in Magnolia field, Gulf of Mexico.

Keevil, G.M., **Peakall, J.**, **Best, J.L.** and **Amos, K.J.** (2006) Flow structure in sinuous submarine channels: Velocity and turbulence structure of an experimental submarine channel. *Mar. Geol.*, **229**, 241–257.

Kneller, B. (1995) Beyond the turbidite paradigm: Physical models for deposition of turbidites and their implications for reservoir prediction. *Geol. Soc. Spec. Publ.*, **94**, 31–49.

Kneller, B., **Bozetti, G.**, **Callow, R.**, **Dykstra, M.**, **Hansen, L.**, **Kane, I.**, **Li, P.**, **McArthur, A.**, **Catharina, A.S.**, **Dos Santos, T.** and **Thompson, P.** (2020)

Architecture, process, and environmental diversity in a late cretaceous slope channel system. *J. Sediment. Res.*, **90**, 1–26.

Kneller, B., **Edwards, D.**, **McCaffrey, W.** and **Moore, R.** (1991) Oblique reflection of turbidity currents. *Geology*, **19**, 250–252.

Kneller, B.C. and **Branney, M.J.** (1995) Sustained high-density turbidity currents and the deposition of thick massive sands. *Sedimentology*, **42**, 607–616.

Kneller, B.C., **Dykstra, M.**, **Fairweather, L.** and **Milana, J.P.** (2016) Mass-transport and slope accommodation: implications for turbidite sandstone reservoirs. *Am. Assoc. Pet. Geol. Bull.*, **100**, 213–235.

Kneller, B.C. and **McCaffrey, W.D.** (2003) The interpretation of vertical sequences in turbidite beds: The influence of longitudinal flow structure. *J. Sediment. Res.*, **73**, 706–713.

Kneller, B.C. and **McCaffrey, W.D.** (1999) Depositional effects of flow nonuniformity and stratification within turbidity currents approaching a bounding slope: deflection, reflection, and facies variation. *J. Sediment. Res.*, **69**, 980–991.

Kremer, C.H., **McHargue, T.**, **Scheucher, L.** and **Graham, S.A.** (2018) Transversely-sourced mass-transport deposits and stratigraphic evolution of a foreland submarine channel system: Deep-water tertiary strata of the Austrian Molasse Basin. *Mar. Pet. Geol.*, **92**, 1–19.

Läuchli, C., **Garcés, M.**, **Beamud, E.**, **Valero, L.**, **Honegger, L.**, **Adatte, T.**, **Spangenberg, J.E.**, **Clark, J.**, **Puigdefàbregas, C.**, **Fildani, A.**, **de Kaenel, E.**, **Hunger, T.**, **Nowak, A.** and **Castelltort, S.** (2021) Magnetostratigraphy and stable isotope stratigraphy of the middle-Eocene succession of the Ainsa basin (Spain):

New age constraints and implications for sediment delivery to the deep waters. Mar Pet Geol. doi: 10.1016/j.marpetgeo.2021.105182

Liang, C., **Xie, X.**, **He, Y.**, **Chen, H.**, **Yu, X.**, **Zhang, W.**, **Mi, H.**, **Lu, B.**, **Tian, D.**, **Zhang, H.**, **Li, M.** and **Zhou, Z.** (2020) Multiple sediment sources and topographic changes controlled the depositional architecture of a palaeoslope-parallel canyon in the Qiongdongnan Basin, South China Sea. *Mar. Pet. Geol.*, **113**, 104161.

Lowe, D.R. (1982) Sediment gravity flows; II, Depositional models with special reference to the deposits of high-density turbidity currents. *J. Sediment. Res.*, **52**, 279–297.

Maier, K.L., **Fildani, A.**, **McHargue, T.R.**, **Paull, C.K.**, **Graham, S.A.** and **Caress, D.W.** (2012) Punctuated deep-water channel migration: High-resolution subsurface data from the lucia chica channel system,offshore California, U.S.A. *J. Sediment. Res.*, **82**, 1–8.

Maier, K.L., **Fildani, A.**, **Paull, C.K.**, **McHargue, T.R.**, **Graham, S.A.** and **Caress, D.W.** (2013) Deep-sea channel evolution and stratigraphic architecture from inception to abandonment from high-resolution Autonomous Underwater Vehicle surveys offshore central California. *Sedimentology*, **60**, 935–960.

Martínez-Doñate, A., **Privat, A.M.L.J.**, **Hodgson, D.M.**, **Jackson, C.A.L.**, **Kane, I.A.**, **Spychala, Y.T.**, **Duller, R.A.**, **Stevenson, C.**, **Keavney, E.**, **Schwarz, E.** and **Flint, S.S.** (2021) Substrate Entrainment, Depositional Relief, and Sediment Capture: Impact of a Submarine Landslide on Flow Process and Sediment Supply. *Front. Earth Sci.*, **9**, 1–23.

Masalimova, L.U., **Lowe, D.R.**, **McHargue, T.I.M.O.T.H.Y.** and **Derksen, R.** (2015)

Interplay between an axial channel belt, slope gullies and overbank deposition in the puchkirchen formation in the Molasse basin, Austria. *Sedimentology*, **62**, 1717–1748.

McArthur, A.D., **Hartley, A.J.**, **Archer, S.G.**, **Jolley, D.W.** and **Lawrence, H.M.** (2016) Spatiotemporal relationships of deep-marine, axial, and transverse depositional systems fromthe synrift Upper Jurassic of the central North Sea. *Am. Assoc. Pet. Geol. Bull.*, **100**, 1469–1500.

McHargue, T., **Pyrcz, M.J.**, **Sullivan, M.D.**, **Clark, J.D.**, **Fildani, A.**, **Romans, B.W.**, **Covault, J.A.**, **Levy, M.**, **Posamentier, H.W.** and **Drinkwater, N.J.** (2011) Architecture of turbidite channel systems on the continental slope: Patterns and predictions. *Mar. Pet. Geol.*, **28**, 728–743.

Menard, H.W. (1955) Deep-Sea Channels, Topography, and Sedimentation. *Am. Assoc. Pet. Geol. Bull.*, **39**, 236–255.

Millington, J.J. and **Clark, J.D.** (1995) The Charo/Arro canyon-mouth sheet system, south-central Pyrenees, Spain: a structurally influenced zone of sediment dispersal. *J. Sediment. Res. B Stratigr. Glob. Stud.*, 443–454.

Morris, E.A., **Hodgson, D.M.**, **Brunt, R.L.** and **Flint, S.S.** (2014a) Origin, evolution and anatomy of silt-prone submarine external levées. *Sedimentology*, **61**, 1734–1763.

Morris, E.A., **Hodgson, D.M.**, **Flint, S.S.**, **Brunt, R.L.**, **Butterworth, P.J.** and **Verhaeghe, J.** (2014b) Sedimentology, stratigraphic architecture, and depositional context of submarine frontal-lobe complexes. *J. Sediment. Res.*, **84**, 763–780.

Moscardelli, L. and **Wood, L.** (2008) New classification system for mass transport complexes in offshoreTrinidad. 73–98.

Mulder, T. and **Alexander, J.** (2001a) The physical character of subaqueous sedimentary density flows and their deposits. *Sedimentology*, **48**, 269–299.

Mulder, T. and **Alexander, J.** (2001b) The physical character of subaqueous sedimentary density flow and their deposits. *Sedimentology*, **48**, 269–299.

Muñoz, J.A. (1992) Evolution of a continental collision belt: ECORS-Pyrenees crustal balanced cross-section. *Thrust Tectonics*, 235–246.

Muñoz, J.A. (2002) The Pyrenees. In: *The Geology of Spain* (Ed. W. Gibbons and T. Moreno), *Geological Society, London*, 370–385.

Muñoz, J.A., **Beamud, E.**, **Fernández, O.**, **Arbués, P.**, **Dinarès-Turell, J.** and **Poblet, J.** (2013) The Ainsa Fold and thrust oblique zone of the central Pyrenees: Kinematics of a curved contractional system from paleomagnetic and structural data. *Tectonics*, **32**, 1142–1175.

Mutti, E. (1977) Distinctive thin-bedded turbidite facies and related depositional environments in the Eocene Hecho Group (South-central Pyrenees, Spain). *Sedimentology*, **24**, 107–131.

Mutti, E., **Luterbacher, H.P.**, **Ferrer, J.** and **Rosell, J.** (1972) Schema stratigrafico e lineamenti di facies del Paleogene marino della zona centrale sudpirenaica tra temp (Catalogna) e Pamplona (Navarra). *Mem. della Soc. Geol. Ital.*, **11**, 391–416.

Mutti, E. and **Normark, W.R.** (1991) An integrated approach to the study of turbidite systems. In: *Seismic facies and sedimentary processes of submarine fans and turbidite systems, Springer, New York, NY.*, 75–106.

Nardin, T.R., **Hein, F.J.**, **Gorsline, D.S.** and **Edwards, B.D.** (1979) A review of mass movement processes, sediment and acoustic characteristics, and contrasts in slope and base-of-slope systems versus canyon- fan- basin floor systems. *Geol. Cont. slopes*, 61–73.

Nijman, W. (1998) Cyclicity and basin axis shift in a piggybank basin: towards modelling of the Eocene Tremp-Ager Basin, South Pyrenees, Spain. 135–162 pp.

Normark, W.R. (1970) Growth patterns of deep- sea fans. *Am. Assoc. Pet. Geol. Bull.*, **54**, 2170–2195.

Nwoko, J., **Kane, I.** and **Huuse, M.** (2020) Mass transport deposit (MTD) relief as a control on post-MTD sedimentation: Insights from the Taranaki Basin, offshore New Zealand. *Mar. Pet. Geol.*, **120**, 104489.

Ortiz-Karpf, A., **Hodgson, D.M.** and **McCaffrey, W.D.** (2015) The role of mass-transport complexes in controlling channel avulsion and the subsequent sediment dispersal patterns on an active margin: The Magdalena Fan, offshore Colombia. *Mar. Pet. Geol.*, **64**, 58–75.

Payros, A., **Tosquella, J.**, **Bernaola, G.**, **Dinarès-Turell, J.**, **Orue-Etxebarria, X.** and **Pujalte, V.** (2009) Filling the North European Early/Middle Eocene (Ypresian/Lutetian) boundary gap: Insights from the Pyrenean continental to deep-marine record. *Palaeogeogr. Palaeoclimatol. Palaeoecol.*, **280**, 313–332.

Peakall, J., **McCaffrey, B.** and **Kneller, B.** (2000) A process model for the evolution, morphology, and architecture of sinuous submarine channels. *J. Sediment. Res.*, **70**, 434–448.

Pemberton, E.A.L., **Hubbard, S.M.**, **Fildani, A.**, **Romans, B.** and **Stright, L.** (2016) The stratigraphic expression of decreasing confinement along a deep-water sediment routing system: Outcrop example from southern Chile. *Geosphere*, **12**, 114–134.

Pickering, K.T. and **Bayliss, N.J.** (2009) Deconvolving tectono-climatic signals in deep-marine siliciclastics, Eocene Ainsa basin, Spanish Pyrenees: Seesaw tectonics versus eustasy. *Geology*, **37**, 203–206.

Pickering, K.T. and **Corregidor, J.** (2005) Mass-transport complexes (MTCs) and tectonic control on basin-floor submarine fans, middle Eocene, South Spanish Pyrenees. *J. Sediment. Res.*, **75**, 761–783.

Pickering, K.T. and **Hiscott, R.N.** (1985) Contained (reflected) turbidity currents from the Middle Ordovician Cloridorme Formation, Quebec, Canada: an alternative to the antidune hypothesis. In: *Deep-Water Turbidite Systems* (Ed. D.A.V. Stow), 89–110.

Pickering, K.T., **Hodgson, D.M.**, **Platzman, E.**, **Clark, J.D.** and **Stephens, C.** (2001) A new type of bedform produced by backfilling processes in a submarine channel, late miocene, Tabernas-Sorbas Basin, se Spain. *J. Sediment. Res.*, **71**, 692–704.

Piper, D.J.W. and **Normark, W.R.** (1983) Turbidite depositional patterns and flow characteristics, Navy submarine fan, California Borderland. *Sedimentology*, **30**, 681–694.

Piper, D.J.W. and **Normark, W.R.** (2001) Sandy fans-from Amazon to Hueneme and beyond. *Am. Assoc. Pet. Geol. Bull.*, **85**, 1407–1438.

Poblet, J., **Muñoz, J.A.**, **Travé, A.** and **Serra-Kiel, J.** (1998) Quantifying the kinematics of detachment folds using three-dimensional geometry: Application to the Mediano anticline (Pyrenees, Spain). *Bull. Geol. Soc. Am.*, **110**, 111–125.

Pohl, F., **Eggenhuisen, J.T.**, **Cartigny, M.J.B.**, **Tilston, M.C.**, **de Leeuw, J.** and **Hermidas, N.** (2020) The influence of a slope break on turbidite deposits: An experimental investigation. Mar Geol. doi: 10.1016/j.margeo.2020.106160

Posamentier, H.W. and **Kolla, V.** (2003) Seismic geomorphology and stratigraphy of depositional elements in deep-water settings. *J. Sediment. Res.*, **73**, 367–388.

Poyatos-Moré, M. (2014) Physical Stratigraphy and Facies Analysis of the Castissent Tecto-Sedimentary Unit. Universitat Autònoma de Barcelona.

Prélat, A., **Hodgson, D.M.** and **Flint, S.S.** (2009) Evolution, architecture and hierarchy of distributary deep-water deposits: a high-resolution outcrop investigation from the Permian Karoo Basin, South Africa. *Sedimentology*, **56**, 2132–2154.

Puigdefàbregas, C. and **Souquet, P.** (1986) Tecto-sedimentary cycles and depositional sequences of the Mesozoic and Tertiary from the Pyrenees. *Tectonophysics*, **129**, 173–203.

Remacha, E. and **Fernández, L.P.** (2003) High-resolution correlation patterns in the turbidite systems of the Hecho Group (South-Central Pyrenees, Spain). *Mar. Pet. Geol.*, **20**, 711–726.

Richardson, S.E.J., **Davies, R.J.**, **Allen, M.B.** and **Grant, S.F.** (2011) Structure and evolution of mass transport deposits in the South Caspian Basin, Azerbaijan. *Basin Res.*, **23**, 702–719.

Rosenbaum, G., **Lister, G.S.** and **Duboz, C.** (2002) Relative motions of Africa, Iberia and Europe during Alpine orogeny. *Tectonophysics*, **359**, 117–129.

Sawyer, D.E., **Flemings, P.B.** and **Nikolinakou, M.** (2014) Continuous deep-seated slope failure recycles sediments and limits levee height in submarine channels.

Geology, **42**, 15–18.

Sawyer, D.E., **Flemings, P.B.**, **Shipp, R.C.** and **Winker, C.D.** (2007) Seismic geomorphology, lithology, and evolution of the late Pleistocene Mars-Ursa turbidite region, Mississippi Canyon area, northern Gulf of Mexico. *Am. Assoc. Pet. Geol. Bull.*, **91**, 215–234.

Scotchman, J.I., **Bown, P.**, **Pickering, K.T.**, **BouDagher-Fadel, M.**, **Bayliss, N.J.** and **Robinson, S.A.** (2015a) A new age model for the middle Eocene deep-marine Ainsa Basin, Spanish Pyrenees. *Earth-Science Rev.*, **144**, 10–22.

Scotchman, J.I., **Pickering, K.T.**, **Sutcliffe, C.**, **Dakin, N.** and **Armstrong, E.** (2015b) Milankovitch cyclicity within the middle eocene deep-marine guaso system, Ainsa Basin, Spanish Pyrenees. *Earth-Science Rev.*, **144**, 107–121.

Sømme, T.O., **Helland-hansen, W.**, **Martinsen, J.** and **Thurmond, J.B.** (2009) Relationships between morphological and sedimentological parameters in source-to-sink systems: a basis for predicting semi-quantitative characteristics in subsurface systems. *Basin Res.*, **21**, 361–387.

Soutter, E.L., **Bell, D.**, **Cumberpatch, Z.A.**, **Ferguson, R.A.**, **Spychala, Y.T.**, **Kane, I.A.** and **Eggenhuisen, J.T.** (2021) The Influence of Confining Topography Orientation on Experimental Turbidity Currents and Geological Implications. Front Earth Sci. doi: 10.3389/feart.2020.540633

Srivastava, S.P. and **Roest, W.R.** (1991) Kinematics of the plate boundaries between Eurasia, Iberia, and Africa in the North Atlantic from the Late Cretaceous to the present. *Geology*, **19**, 613–616.

Stevenson, C.J., **Jackson, C.A.L.**, **Hodgson, D.M.**, **Hubbard, S.M.** and **Eggenhuisen,**

J.T. (2015) Deep-water sediment bypass. *J. Sediment. Res.*, **85**, 1058–1081.

Stevenson, C.J., **Peakall, J.**, **Hodgson, D.M.**, **Bell, D.** and **Privat, A.** (2020) Tb or not tb: banding in turbidite sandstones. *J. Sediment. Res.*, **90**, 821–842.

Steventon, M.J., **Jackson, C.A.-L.**, **Johnson, H.D.**, **Hodgson, D.M.**, **Kelly, S.**, **Omma, J.**, **Gopon, C.**, **Stevenson, C.** and **Fitch, P.** (2021) Evolution of a sand-rich submarine channel-lobe system and impact of mass-transport and transitional flow deposits on reservoir heterogeneity: Magnus Field, northern North Sea. *Pet. Geosci.*, petgeo2020-095.

Sumner, E.J., **Amy, L.A.** and **Talling, P.J.** (2008) Deposit structure and processes of sand deposition from decelerating sediment suspensions. *J. Sediment. Res.*, **78**, 529–547.

Talling, P.J., **Masson, D.G.**, **Sumner, E.J.** and **Malgesini, G.** (2012) Subaqueous sediment density flows: Depositional processes and deposit types. *Sedimentology,* **59**, 1937–2003.

Tek, D.E., **McArthur, A.D.**, **Poyatos-Moré, M.**, **Colombera, L.**, **Patacci, M.**, **Craven, B.** and **McCaffrey, W.D.** (2021) Relating seafloor geomorphology to subsurface architecture: How mass-transport deposits and knickpoint-zones build the stratigraphy of the deep-water Hikurangi Channel. *Sedimentology*, **68**, 3141–3190.

Tek, D.E., **Poyatos-Moré, M.**, **Patacci, M.**, **McArthur, A.D.**, **Colombera, L.**, **Cullen, T.M.** and **McCaffrey, W.D.** (2020) Syndepositional tectonics and mass-transport deposits control channelized, bathymetrically complex deep-water systems (Aínsa depocenter, Spain). 729–762 pp.

Terlaky, V. and **Arnott, R.W.C.** (2016) The control of terminal-splay sedimentation on depositional patterns and stratigraphic evolution in avulsion-dominated, unconfined, deep-marine basin-floor systems. *J. Sediment. Res.*, **86**, 786–799.

Thomson, K.D., **Stockli, D.F.**, **Clark, J.D.**, **Puigdefàbregas, C.** and **Fildani, A.** (2017) Detrital zircon (U-Th)/(He-Pb) double-dating constraints on provenance and foreland basin evolution of the Ainsa Basin, south-central Pyrenees, Spain. *Tectonics*, **36**, 1352–1375.

Tinterri, R. (2011) Combined flow sedimentary structures and the genetic link between sigmoidal-and hummocky-cross stratification. *GeoActa*, **10**, 43–85.

Tinterri, R. and **Muzzi Magalhaes, P.** (2011) Synsedimentary structural control on foredeep turbidites: An example from Miocene Marnoso-arenacea Formation, Northern Apennines, Italy. *Mar. Pet. Geol.*, **28**, 629–657.

Valdez, V., **Milana, J.P.**, **Sobiesiak, M.S.** and **Kneller, B.** (2019) The Carboniferous MTD Complex at La Peña Canyon, Paganzo Basin (San Juan, Argentina). In: *Submarine Landslides: Subaqueous Mass Transport Deposits from Outcrops to Seismic Profiles*, 105–116.

van Toorenenburg, K.A., **Donselaar, M.E.**, **Noordijk, N.A.** and **Weltje, G.J.** (2016) On the origin of crevasse-splay amalgamation in the Huesca fluvial fan (Ebro Basin, Spain): Implications for connectivity in low net-to-gross fluvial deposits. *Sediment. Geol.*, **343**, 156–164.

Zhong, G. and **Peng, X.** (2021) Transport and accumulation of plastic litter in submarine canyons—The role of gravity flows. *Geology*, **49**, 581–586.